



Inverse design of optical metasurfaces

Final report P&O
May 2023

by Liam Fallik,
Laura Vallejo and
Willem Vanmoerkerke

Supervisors: Dr. ir. Bruno Figeys and Dr. Ugo Stella

Academic year 2022-2023

Abstract

Optical metasurfaces are a novel class of structures, consisting in cleverly designed patterns imprinted in a flat material and enabling the exploitation of unique properties at smaller scales than conventional optics. However, these structures possess many degrees of freedom, which make them difficult to design directly. In this report, first a mathematical model to investigate the properties and the physical limit of metasurfaces is developed. Then this theory is used to design these metasurfaces directly. Finally, the optimization of metasurfaces using the adjoint method of inverse design is presented, this is a powerful photonics topology optimization method. This method is applied to various problems, namely the design of a focusing lens, of a frequency splitter that focuses different wavelengths on different points in space, and of a retroreflector which reflects a light ray in its incident direction.

Keywords: optical metasurface, metalens, adjoint method, inverse design

Acknowledgements

First and foremost we need to thank Bruno and Ugo. Without their daily guidance and dedicated involvement in every aspect of the project, this report would have never been accomplished. We learned a lot from cooperating in the research they have been doing for years, from the extensive knowledge they have about the topic to the advice they gave about doing research in general.

We would also like to thank the IT support of Imec for helping us receive access to the Imec servers that were essential to perform the simulations.

List of Abbreviations and Symbols

Abbreviations	
2D	Two-Dimensional
3D	Three-Dimensional
a.u.	Arbitrary Unit
FDTD	Finite-Difference Time-Domain
FOM	Figure Of Merit
FWHM	Full-Width at Half-Max
MFS	Minimum Feature Size
NA	Numerical Aperture
PML	Perfectly Matched Layer

Latin Symbols	
A	Adjoint field
d	Layer thickness
E	Electric field
E_z	z -polarized electric field
e	Euler's number
F	Objective function
H	Magnetic field
I_f	Intensity at the focal point
i	The imaginary unit
J	Current
f	Focal length
H	Magnetic field
k	The wave number $k = \frac{2\pi}{\lambda}$
n	Refractive index
P	Hat function
r	Distance between a point (x, y) behind the lens and a point (x', y') on the focal plane
r'	Distance between a point (x, y) behind the lens and the focal point
τ_1	Linear transformation of the lens on the fields
τ_2	Linear transformation over a distance in vacuum
U_0	Field of an incoming plane wave
U_1	Field behind the lens
U_2	Field at the focal plane
w	Width of the lens
X	Amount of layers
x	First spatial coordinate behind the lens
x'	First spatial coordinate on the focal plane
y	Second spatial coordinate behind the lens
y'	Second spatial coordinate on the focal plane
z	Third spatial coordinate

Greek Symbols	
α	Azimuth in polar coordinates
β	Parameter in Hat function that determines binarization
δ	Magnetiv resistivity
ϵ	Dielectric constant
θ	Angle between \vec{r} and the normal to the

λ	lens
$\overrightarrow{\lambda^{-1}}$	Wavelength of light
μ	Reverse wavelength vector
π	Magnetic permeability
π	Area of the unit circle
ρ	Material distribution
ϕ	Phase-shift of the electric field
ϕ_0	Constant phase off-set
ϕ_1	Phase of the field behind the lens
ϕ_{fi}	Phase at the focal point from an infinitesimal light source
$\overrightarrow{\phi}$	Phase vector
$\overrightarrow{\psi}$	Element of \mathbb{R}^m
Ω	Volume

List of Figures

1.1	Optical properties of materials (Zhu and Liu, 2023).	1
1.2	Mathematical model of a lens.	2
1.3	Representation of the Rayleigh-Sommerfeld integral.	4
1.4	Intensity at the focal point relative to the source (I_f) in function of the distance between the lens and the focal point (f) for (a) a 2D lens with width $w = 10 \mu\text{m}$ and (b) a circular lens with diameter $w = 10 \mu\text{m}$ and a rectangular lens with width $w = 10 \mu\text{m}$ for light of wavelength $\lambda = 0.6 \mu\text{m}$. The intensity reaches a maximum $I_f = 26.3$ at $f = 2.74 \mu\text{m}$ for the 2D lens, $I_f = 444$ at $f = 2.52 \mu\text{m}$ for the circular lens and $I_f = 555$ at $f = 2.83 \mu\text{m}$ for a rectangular lens.	5
1.5	The intensity at the focal line/plane for a (a) 2D and (b) 3D lens. The maximum relative intensity is $I_f(0) = 20.99$ for the 2D lens and $I_f(0, 0) = 389.96$ for the 3D lens, while the first zero is at $x = 0.44 \mu\text{m}$ for the 2D lens and at $x = 0.474 \mu\text{m}$ for the 3D lens. Finally, the full-width at half-max (FWHM) is $0.402 \mu\text{m}$ for the 2D lens and $0.424 \mu\text{m}$ for the 3D lens. Mind the different scale for the two figures.	6
1.6	Example of a manufacturable metasurface with a minimum feature size of 90 nm. Light gray: SiO_2 and black: TiO_2	7
1.7	Illustration of the modulation of the phase by a metasurface with SiO_2 (light gray) and TiO_2 (black) in an environment of air (white).	7
1.8	Representation of the required phases to achieve optimal control.	8
1.9	Representation of the required phases to achieve optimal control for uniform thicknesses for (a) two layers and (b) three layers.	9
1.10	Representation of the required phases to achieve optimal control for exponential thicknesses for (a) two layers and (b) three layers. SiO_2 is colored light gray and TiO_2 is colored black.	10
1.11	(a) method to design a lens and (b) comparison between direct design and inverse design. SiO_2 is colored light gray and TiO_2 is colored black.	10
1.12	The required phases for a non-periodic 2D frequency splitter of red (650 nm) and blue light (470 nm) with width $w = 10 \mu\text{m}$, focal points at a distance $f = 6 \mu\text{m}$ and both $3 \mu\text{m}$ off-axis. (a) the phase in function of the distance and (b) the values that the phase vector $\vec{\phi} = (\phi_{\text{blue}}, \phi_{\text{red}})$ takes.	11
1.13	Schematic of the problem statement to determine the optimal thicknesses for four layers and two frequencies.	12
1.14	Inverse design methodology.	12
1.15	Schematic of direct and adjoint simulation runs (Lalau-Keraly et al., 2013).	13
1.16	Hat filter $P(x)$ for different values of β	14
1.17	Yee cell geometry (Narayan et al., 2017).	16
2.1	Structure implemented in Meep.	18
2.2	Random sampling optimization: (a) a number of random samples are chosen, (b) all samples are optimized locally and (c) the best optimized sample is the optimal structure.	19
2.3	An example of the figure of merit for 30 different samples.	19
2.4	Random sampling optimization: (a) the starting structure is optimized locally, (b) from this optimum, some (2) random steps are taken (red arrows) and these new structures are again optimized locally. The best of all structures is chosen (c) the β value (see section 1.4.1) of the structure is increased, which changes the energy landscape, (d) again a local optimization is executed and (e) random steps are taken (red arrows) and these new structures are again optimized locally. The best of all structures is chosen. If the β has reached the final value, this structure is also the optimal design, if not, the steps are repeated from c.	20

2.5	An example of the figure of merit in function of the iteration step for a stochastic optimization algorithm. The red circles mark the initial optimization after the β is increased, before a random step is taken.	20
2.6	(a) Relative intensity at the focal point for the best design achieved in function of the minimum feature size for one layer and five layers (uniform thicknesses). Width $w = 10 \mu\text{m}$, focal distance $f = 6 \mu\text{m}$, average of wavelengths $\lambda = 550 \text{ nm}, 600 \text{ nm}$ and 650 nm . (b) The resulting structure, intensity in the XY-plane and intensity on the focal line for a selection of the minimum feature sizes for one layer and light with a wavelength of 600 nm . The blue circle is plotted to represent the minimum feature size.	21
2.7	Relative intensity at the focal point for the best design achieved for a different number of layers. Width $w = 10 \mu\text{m}$, focal length $f = 6 \mu\text{m}$, average of wavelengths $\lambda = 550 \text{ nm}, 600 \text{ nm}$ and 650 nm . (a) Minimum feature size of 90 nm and (b) minimum feature of 10 nm	22
2.8	Optimal structure of the metalens with width $w = 10 \mu\text{m}$, $f = 6 \mu\text{m}$ for wavelengths $\lambda = 550, 600, 650 \text{ nm}$. (a) 1 layer, (b) 2 layers with uniform thicknesses, (c) 2 layers with exponential thicknesses, (d) 3 layers with uniform thicknesses, (e) 3 layers with exponential thicknesses, (f) 4 layers with uniform thicknesses, (g) 4 layers with exponential thicknesses, (h) 5 layers with uniform thicknesses, (i) 6 layers with uniform thicknesses.	22
2.9	Optimal structure of the metalens with width $w = 10 \mu\text{m}$, $f = 6 \mu\text{m}$ and a minimum feature size of 10 nm for wavelengths $\lambda = 550, 600, 650 \text{ nm}$. (a) 1 layer, (b) 2 layers with uniform thicknesses, (c) 2 layers with exponential thicknesses, (d) 4 layers with uniform thicknesses and (e) 4 layers with exponential thicknesses.	23
2.10	(a) The intensity at the focal point in function of the focal length (f). The line represents the theoretical value, as derived in section 1.2, while the red dots represent the values obtained with inverse design. (b) The real part of the electric field and (c) the intensity map (with arbitrary unit) for a focal length of $1 \mu\text{m}$	23
2.11	Optimal design of a lens of width $w = 10 \mu\text{m}$, MFS of 10 nm , focal length $f = 1 \mu\text{m}$ and light of wavelengths $550 \text{ nm}, 600 \text{ nm}$ and 650 nm	24
2.12	Relative intensity at the focal point depending on the number of layers and the type of design. Width $w = 10 \mu\text{m}$, focal length $f = 6 \mu\text{m}$, wavelength $\lambda = 600 \text{ nm}$	24
2.13	Optimal designs of a lens with width $w = 10 \mu\text{m}$, MFS of 90 nm , focal length $f = 6 \mu\text{m}$ for wavelength $\lambda = 600 \text{ nm}$. (a) 1 layer, direct design, (b) 1 layer, inverse design, (c and d) 2 uniform layers, direct design, bottom and top layer respectively. (e and f) 2 uniform layers, inverse design, bottom and top layer respectively. (g and h) 2 exponential layers, inverse design, bottom and top layer respectively.	25
3.1	Schematic of a conventional photodetector array (a) and metalens color splitter (b) (Miyata et al., 2021).	26
3.2	Cross-section of an OLED device with microlenses (Motoyama et al., 2019).	26
3.3	1-layered metasurface focusing two colors. Thickness = $0.25 \mu\text{m}$, focal point = $7 \mu\text{m}$	27
3.4	4-layered metasurface focusing three colors. Thicknesses = $0.5, 0.445, 0.35$ and $0.216 \mu\text{m}$, focal point = $4 \mu\text{m}$	28
3.5	Bayer pattern for a pixel array.	29
3.6	Schematic of the Bayer pattern with computational cell. The boundaries of the computational cell are represented in purple and the symmetry lines in yellow. The hatched area is the effective computational cell, after symmetrization.	29
3.7	2-frequency splitter, quarter of the total computational cell. Thicknesses = $0.487, 0.299, 0.230, 0.138 \mu\text{m}$, focal point = $3 \mu\text{m}$. (a, b): Relative intensity at the focal point for blue and red, respectively. (c-f): metasurface layer structure.	30

3.8	3-frequency splitter, quarter of the total computational cell. Thicknesses = 0.4, 0.365, 0.298, 0.186 μm , focal point = 3 μm . (a-c): Relative intensity at the focal point for blue, red and green respectively. (d-g): metasurface layer structure.	31
3.9	Focusing power as a function of wavelength on blue, red and green pixels.	31
4.1	Schematic representation of: (a) bulky corner reflector. (b) cascaded metasurface (Yan et al., 2018).	32
4.2	Schematic representation of: a) reflection by a mirror, a planar retroreflector and a gradient metasurface. b) planar retroreflector composed of two metasurfaces (Arbabi et al., 2017).	32
4.3	Cascaded retroreflector, optimization design.	33
4.4	Optimized retroreflectors: Final design and E_z fields with metasurfaces I and II optimized at the same time for 5°, 10° and 15° source angle.	34
4.5	Optimized retroreflectors: Final design and E_z fields with dual metasurfaces, jointly optimized for a 15° source angle.	35
4.6	Optimized retroreflector for multiple angles: Final design and E_z fields with two metasurfaces, jointly optimized for 10° and 20° source angles.	36
4.7	Relative incidence vs angles of incidence for the retroreflector optimized for two angles	36
4.8	Zoomed-in intensity profile at 10° and 20°.	37
B.1	Integration region for a square lens with width w	43
B.2	Taylor series approximations for the integrand. The zeroth order Taylor expansion would give the same solution as the circular lens. The fourth/fifth order Taylor expansion is used to approximate the integral.	44

Contents

Abstract	ii
Acknowledgement	iii
List of Abbreviations and Parameters	iv
List of Figures	vi
1 Introduction	1
1.1 Optical metasurfaces	1
1.2 Mathematical model	2
1.2.1 A metasurface presented as a linear transformation	2
1.2.2 Quantification of the optimal 3D lens	3
1.2.3 Quantification of the optimal 2D lens	5
1.3 Direct design of metasurfaces	6
1.3.1 Phase modulation in practice	6
1.3.2 Direct design of a lens	8
1.3.3 Direct design of a frequency splitter	10
1.4 Inverse design	12
1.4.1 Adjoint method	13
1.5 Simulation	14
1.5.1 Finite Difference Time Domain (FDTD) Method	14
1.5.2 MEEP	16
1.5.3 Far Fields	16
1.5.4 Exploiting parallelism	17
2 Focusing lens	18
2.1 Problem Statement	18
2.2 Optimization algorithm	19
2.3 Results for a 2D metalens	20
2.4 Results for a 3D metalens	24
3 Frequency splitter	26
3.1 2D splitter	27
3.1.1 2 frequencies	27
3.1.2 3 frequencies	28
3.2 3D splitter	28
4 Retroreflector	32

4.1	Problem statement	33
4.2	Results	34
4.2.1	First approach: Metasurfaces I and II optimized at the same time	34
4.2.2	Second approach: Metasurfaces optimized in series	35
4.2.3	Multiple angles	35
5	Conclusion	38
References		39
A	Fresnel approximation	40
B	Analytical derivation of the intensity at the focal point	42
B.1	Intensity for a circular lens	42
B.2	Intensity for a rectangular lens	42
C	Gaussian source in Meep	45
D	Taylor series	46
E	Metropolis Monte Carlo code for the thickness optimization	47

1 Introduction

To enhance key technologies, like imaging, sensors, solar cells, optical communication, advanced displays and virtual reality, there is an increasing need for optical elements at the nanoscale that can be integrated in microelectronics. This problem is solved by optical metasurfaces, or flat optics, that modifies light with subwavelength structures and is compatible with CMOS processing. The development of these structures has long relied on direct design. This design method relies on an intuitive approach based on a priori known physical effects and can be improved by tuning a small set of parameters. This approach is very challenging with increasing complexity. Inverse design on the other hand takes a more algorithmic approach. It regards the required characteristics as a function of the structure and as a result an optimization algorithm can be used to find the optimal structure. (Molesky, Lin, Piggott, et al., 2018)

This report starts with an introduction that explains optical metasurfaces in more detail, develops a mathematical model and explores the theoretical limits that can be achieved. Also direct design is explored as a reference to the inverse design structures later in the report. The introduction is concluded with an outset of inverse design and the simulation methods used. Subsequently, the inverse design of three applications is discussed: a focusing lens, a color splitter and a retroreflector. Finally, the report is completed with some concluding remarks.

1.1 Optical metasurfaces

The interaction between the molecular composition of a material and the incident electromagnetic (EM) waves defines the optical properties of a material, like its permittivity and permeability. For all natural materials, permittivity, permeability or both are positive quantities, meaning that the electrical field, magnetic field and wave vector of an EM wave follow the right-handed rule when propagating through them, as shown in Figure 1.1. However, it is possible to create materials with simultaneously negative permittivity and permeability (left-handed materials), that exhibit a phase velocity in an opposite direction to the Pointing vector. These artificial materials, known as metamaterials, are designed with subwavelength structure arrays. The architecture of these structures, combined with the chemical composition of the material, determine the unique and tailored functionality of the metamaterial (Zhu and Liu, 2023).

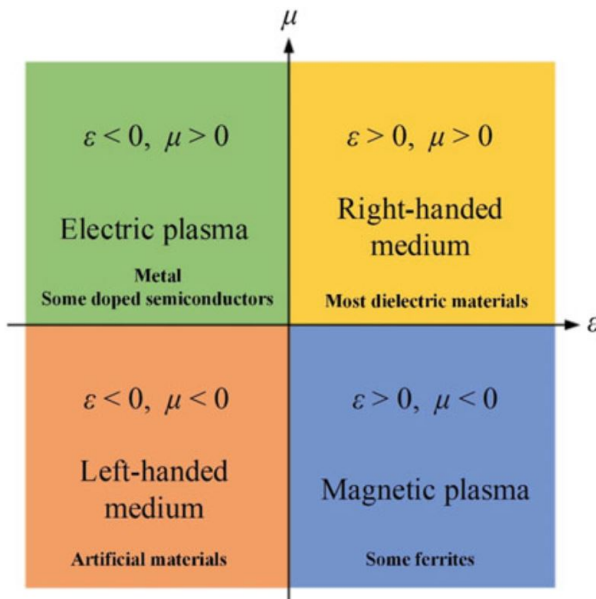


Figure 1.1: Optical properties of materials (Zhu and Liu, 2023).

2D arrangements of metamaterials are metasurfaces. Among them, the optical metasurfaces are diffractive optical elements engineered with subwavelength structures capable of modifying the phase, polarization and amplitude of a propagating EM wave. These interesting capabilities have led to the use of the metasurfaces in

different applications, such as beam deflection, beam splitting, polarization elements, flat lenses, retroreflectors, waveplates, holograms, and so forth (Yan et al., 2018). Metasurfaces are usually planar, optically thin, and can be manufactured by 2D fabrication technologies.

Most of the metasurfaces have been studied in a electromagnetic range from visible light to microwave. However, recent research have demonstrated that they are also capable of tailoring the wavefront of acoustic waves, broadening the application field of these devices (Zhu and Liu, 2023). In summary, metasurfaces, particularly optical metasurfaces, have a great potential for advancing device designs beyond the capabilities of natural materials. They offer numerous advantages, including compact size, high operating speed, cost-effectiveness, and reduced power consumption, among others, enabling the development of innovative devices with superior performance in various applications.

1.2 Mathematical model

This section gives the mathematical background related to diffraction and lenses. This background is required for direct design of optical metasurfaces and is also the basis for quantifying the results of the inverse designed structures in section 2. In the next section, the mathematical background will be used to determine analytically the optimal structure for a lens and a frequency splitter. The section start with the mathematical model for a lens and the model will then be generalised for a frequency splitter, considering that this is a structure that focuses different frequencies at different off-axis focal points.

1.2.1 A metasurface presented as a linear transformation

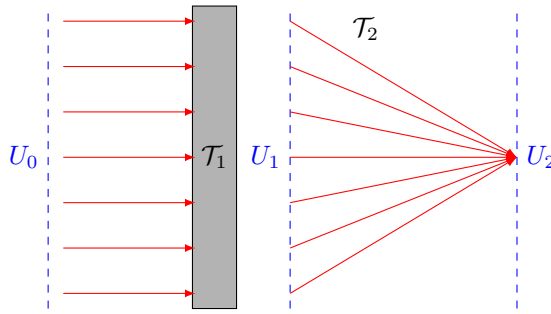


Figure 1.2: Mathematical model of a lens.

Figure 1.2 visualizes the mathematical model. The incident wavefront is characterised by a field U_0 . In this case, it is assumed that the incident light wave is a normalized z-polarised plane wave. This means that the field is constant in the plane with an absolute value of 1. As an off-set to the phase is irrelevant, the phase of the incident wavefront is ignored. Also the light passing next to the lens is ignored and set to 0.

$$U_0(x, y) = \begin{cases} 1 & |x|, |y| \leq \frac{w}{2} \\ 0 & |x|, |y| > \frac{w}{2} \end{cases} \quad (1)$$

The lens performs a linear transformation \mathcal{T}_1 on the passing wavefront. In general, the outcoming wavefront is presented in equation 2.

$$U_1 = \mathcal{T}_1(U_0) \quad (2)$$

The linear transformation \mathcal{T}_1 is determined by the structure of the lens. In direct design, the field U_1 is optimised (under a few constraints which will be elaborated later) to maximise the focusing efficiency in the focal plane. From the field U_1 the linear transformation \mathcal{T}_1 is calculated. Finally the transformation \mathcal{T}_1 determines the structure of the lens. Before the implementation of direct design can be discussed further, the relation between the field coming out of the lens U_1 and the field at the focal plane U_2 has to be determined.

The outcoming wavefront propagates through space and is observed at the focal plane. At the focal plane, the observed field is called U_2 . The relation between the field U_1 and U_2 is again expressed by a linear transformation

\mathcal{T}_2 .

$$U_2 = \mathcal{T}_2(U_1) \quad (3)$$

The Huygens–Fresnel principle states that every point on a wavefront is itself the source of spherical wavelets and that these wavelets interfere with each other (Fresnel, 1819; Huygens, 1912). So, intuitively it is expected that to maximise the intensity in the focal point, i.e the value of $|U_2(x = 0, y = 0)|^2$, all wavelets coming from U_1 need to interfere constructively. The phase at the focal point due to an infinitesimal source on the U_1 wavefront (ϕ_{fi}) is given by:

$$\phi_{fi} = \phi_1(x, y) + 2\pi \frac{r'}{\lambda} \pmod{2\pi} \quad (4)$$

$$= \phi_1(x, y) + 2\pi \frac{\sqrt{f^2 + x^2 + y^2}}{\lambda} \pmod{2\pi} \quad (5)$$

With $\phi_1(x, y)$ the phase of the infinitesimal source on the U_1 wavefront on position (x, y) , r' the distance between the point on U_1 and the focal point, λ the wavelength of the light, x and y the coordinates of this point on U_1 and f the focal length. Notice that only the modulo of the phase is important. If the constructive interference is required to maximise the intensity at the focal point, ϕ_{fi} should be constant for all positions (x, y) .

$$\phi_{fi} = \phi_0 = \phi_1(x, y) + 2\pi \frac{\sqrt{f^2 + x^2 + y^2}}{\lambda} \pmod{2\pi} \quad (6)$$

$$\phi_1(x, y) = \phi_0 - 2\pi \frac{\sqrt{f^2 + x^2 + y^2}}{\lambda} \pmod{2\pi} \quad (7)$$

Equation 7 shows the required phase of the field at every point behind the lens to have constructive interference at the focal point. It is assumed that the lens is infinitely thin and perfectly transmitting and thus that it only modulates the phase, this means that the magnitude of the field is equal to the magnitude of the field of the incoming plane wave. Equation 7 can easily be generalised for a frequency splitter. In this case the wavefronts of n different wavelengths $\lambda_{i=1,\dots,n}$ need to interfere constructively in n different focal points $(x_{i=1,\dots,n}, y_{i=1,\dots,n}, f_{i=1,\dots,n})$.

$$\begin{cases} \phi_{11}(x, y) = \phi_{01} - 2\pi \frac{\sqrt{f_1 + (x - x_{f1})^2 + (y - y_{f1})^2}}{\lambda_1} \pmod{2\pi} \\ \phi_{12}(x, y) = \phi_{02} - 2\pi \frac{\sqrt{f_2 + (x - x_{f2})^2 + (y - y_{f2})^2}}{\lambda_2} \pmod{2\pi} \\ \dots \\ \phi_{1n}(x, y) = \phi_{0n} - 2\pi \frac{\sqrt{f_n + (x - x_{fn})^2 + (y - y_{fn})^2}}{\lambda_m} \pmod{2\pi} \end{cases} \quad (8)$$

In this case a different phase behind the lens ($\phi_{1i}(x, y)$) is required for every wavelength (λ_i). The structure of the metasurface needed to acquire the phase imposed by equation 7 or 8 is discussed in section 1.3. First, the next section quantifies the theoretical limit that can be achieved with these metasurfaces.

1.2.2 Quantification of the optimal 3D lens

The analysis above states that to maximise the intensity at the focal point, constructive interference is required. However, the value of the intensity at the focal point and at the focal plane in general is still unknown. The field at the focal plane can be calculated with the Rayleigh-Sommerfeld integral¹ (Mehrabkhani and Schneider, 2017).

$$U_2(x', y') = -\frac{1}{2\pi} \iint_S U_1(x, y) \left(ik - \frac{1}{r} \right) \frac{e^{ikr} \cos(\theta)}{r} dx dy, \quad \text{with } r = \sqrt{(x - x')^2 + (y - y')^2 + f^2} \quad (9)$$

¹From the Rayleigh-Sommerfeld integral it can be seen that the previous analysis for the optimal phase change is not completely correct. In the Rayleigh-Sommerfeld integral, both $U_1(x, y)$ and e^{ikr} are complex with modulus 1 (assuming there is no absorption, generation or reflection in the lens). However, also $(ik - \frac{1}{r})$ is a complex number, with a phase that depends on r . As discussed, $U_1(x, y)$ should be chosen in such a way that the phase is constant to achieve constructive interference. In the discussion above, the phase of $U_1(x, y)e^{ikr}$ was made constant, nevertheless from this integral it is clear that the phase of $U_1(x, y)e^{ikr} (ik - \frac{1}{r})$ should be made constant. However, as typically $k = \frac{2\pi}{\lambda} \approx 10.5 \text{ } \mu\text{m}^{-1}$ and $\frac{1}{r} \geq \frac{1}{f} \approx 0.167 \text{ } \mu\text{m}^{-1}$ in this study, it follows that $k \gg \frac{1}{r}$ and the phase variation of $(ik - \frac{1}{r})$ can be neglected.

With x' and y' the coordinates in the focal plane, $k = \frac{2\pi}{\lambda}$ the wave number, r the distance between the point (x, y) on the lens plane and the point (x', y') on the focal plane and θ the angle between the vector \vec{r}' connecting (x, y) and (x', y') and the normal to the lens. These variables are presented (in 2D) in Figure 1.3.

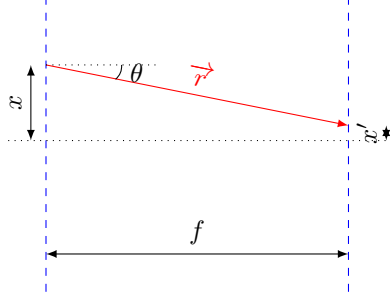


Figure 1.3: Representation of the Rayleigh-Sommerfeld integral.

For the optimal lens, assuming that no light passes aside the lens, the field $U_1(x, y)$ according to equation 7 is given by:

$$U_1(x, y) = \begin{cases} e^{i\phi_1(x, y)} & |x| \text{ and } |y| \leq \frac{w}{2} \\ 0 & |x| \text{ or } |y| > \frac{w}{2} \end{cases} \quad (10)$$

$$= \begin{cases} e^{i(\phi_0 - 2\pi \frac{\sqrt{f^2 + x^2 + y^2}}{\lambda} \pmod{2\pi})} & |x| \text{ and } |y| \leq \frac{w}{2} \\ 0 & |x| \text{ or } |y| > \frac{w}{2} \end{cases} \quad (11)$$

From here on, the off-set ϕ_0 and the modulo are dropped as the phase off-set is irrelevant.

$$U_1(x, y) = \begin{cases} e^{-2\pi i \frac{\sqrt{f^2 + x^2 + y^2}}{\lambda}} & |x| \text{ and } |y| \leq \frac{w}{2} \\ 0 & |x| \text{ or } |y| > \frac{w}{2} \end{cases} \quad (12)$$

$$= \begin{cases} e^{-ikr'}, & \text{with } r' = \sqrt{x^2 + y^2 + f^2} \quad |x| \text{ and } |y| \leq \frac{w}{2} \\ 0 & |x| \text{ or } |y| > \frac{w}{2} \end{cases} \quad (13)$$

Equation 12 can be filled into equation 9.

$$U_2(x', y') = -\frac{1}{2\pi} \iint_S e^{-ikr'} \left(ik - \frac{1}{r} \right) \frac{e^{ikr} \cos(\theta)}{r} dx dy \quad (14)$$

$$= -\frac{1}{2\pi} \iint_S \left(ik - \frac{1}{r} \right) \frac{e^{ik(r-r')} \cos(\theta)}{r} dx dy \quad (15)$$

Very often the Fresnel approximation $r \approx f$ is made in literature, which simplifies the integral (Konijnenberg et al., 2021). However, in this case, high NA optical metasurfaces are studied and typical values are $f = 6 \mu\text{m}$, $w = 10 \mu\text{m}$ and thus $r_{max} = \sqrt{f^2 + (\frac{w}{2})^2} = 7.81 \mu\text{m}$. As a result, the Fresnel approximation is a very coarse approximation for the lenses studied and the exact integral needs to be calculated. The Fresnel approximation is elaborated in appendix A. The exact integral can be calculated numerically and the results are shown in Figure 1.5b. Except at the focal point, the integral is simplified and can be calculated analytically. Both for a circular lens as a rectangular lens the calculation is made in appendix B. For a circular lens with diameter w , focal length f and light with wavelength λ the relative intensity at the focal point ($I_f(0, 0)$) is given by:

$$I_f(0, 0) = \left\{ \frac{\pi f}{\lambda} \ln \left[1 + \left(\frac{w}{2f} \right)^2 \right] \right\}^2 \quad (16)$$

For $f = 6 \mu\text{m}$, $w = 10 \mu\text{m}$ and $\lambda = 0.6 \mu\text{m}$, the optimal intensity relative to the intensity of the source is equal

to $I_f = 274.5$. For the rectangular lens, the intensity at the focal point is given by:

$$I_f(0,0) \approx \frac{\pi^2 f^2}{\lambda^2} \left\{ \ln \left[1 + \left(\frac{w}{2f} \right)^2 \right] + \frac{1}{1 + \left(\frac{2f}{w} \right)^2} \frac{\pi^2}{48} + \frac{1 + 4 \left(\frac{2f}{w} \right)^2}{\left[1 + \left(\frac{2f}{w} \right)^2 \right]^2} \frac{\pi^4}{7680} \right\}^2 \quad (17)$$

For $f = 6 \mu\text{m}$, $w = 10 \mu\text{m}$ and $\lambda = 0.6 \mu\text{m}$, the optimal intensity relative to the intensity of the source is equal to $I_f(0,0) = 389.96$. Interestingly, the maximum intensity is very dependent on the focal distance f . The intensity is plotted as a function of f in Figure 1.4b. Also the results for 2D which can be calculated numerically from the 2D analysis discussed further are already given in Figure 1.4a. In all cases the intensity goes down for increasing f for large f . This was expected as the numerical aperture (NA) decreases with increasing f . It can also be seen from the Rayleigh-Sommerfeld integral in equation 9, the further the focal point, the larger the value of r will be in the denominator, decreasing the efficiency. Physically this corresponds to diluted light waves at further distances. However, what might be more surprising is the decreasing intensity for very small focal lengths. This is caused by the cosine in the Rayleigh-Sommerfeld integral (and later the logarithm in equation 17). For smaller values of f , the light waves need to be scattered at larger angles and thus $\cos(\theta)$ decreases in the numerator of the Rayleigh-Sommerfeld integral leading to lower intensities. For a circular lens with diameter $w = 10 \mu\text{m}$ and wavelength $\lambda = 0.6 \mu\text{m}$, an optimum is reached at $f = 2.52 \mu\text{m}$ with a relative intensity of $I_f = 444$. While for a rectangular lens with width $w = 10 \mu\text{m}$, an optimum is reached at $f = 2.83 \mu\text{m}$ with a relative intensity of $I_f = 555$.

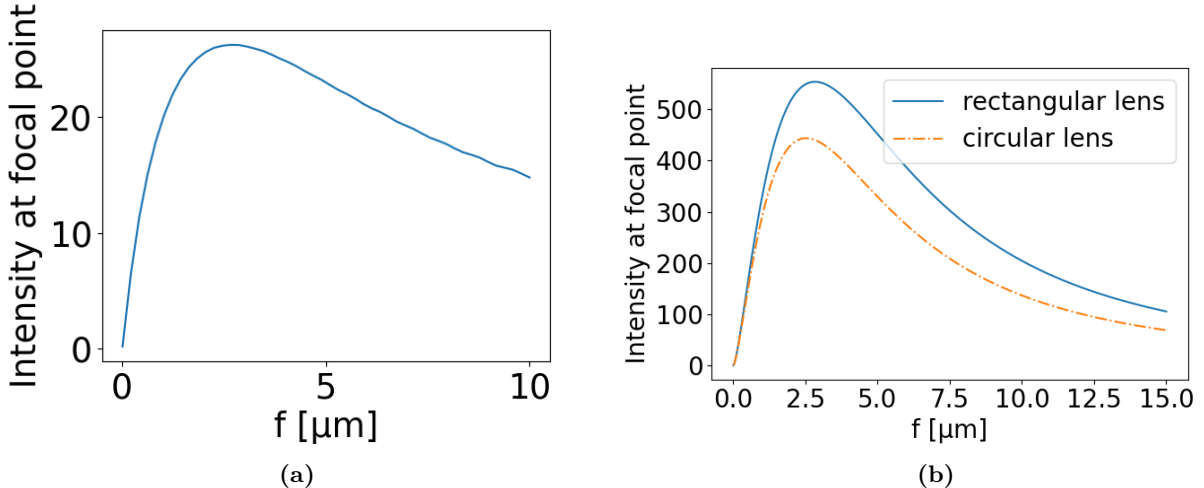


Figure 1.4: Intensity at the focal point relative to the source (I_f) in function of the distance between the lens and the focal point (f) for (a) a 2D lens with width $w = 10 \mu\text{m}$ and (b) a circular lens with diameter $w = 10 \mu\text{m}$ and a rectangular lens with width $w = 10 \mu\text{m}$ for light of wavelength $\lambda = 0.6 \mu\text{m}$. The intensity reaches a maximum $I_f = 26.3$ at $f = 2.74 \mu\text{m}$ for the 2D lens, $I_f = 444$ at $f = 2.52 \mu\text{m}$ for the circular lens and $I_f = 555$ at $f = 2.83 \mu\text{m}$ for a rectangular lens.

In many applications, the width of the lens w is fixed by the design. For example in a μ LED array, the width of the metasurfaces is fixed by the pitch of the μ LEDs. However, the distance between the LEDs and the lenses is not always determined a priori. As a consequence, the focal distance f can be used as another parameter to optimize the design.

1.2.3 Quantification of the optimal 2D lens

For a 2D metalens a similar calculation can be made. The optimal field is then

$$U_1(x) = e^{i\phi_1(x)} \quad (18)$$

$$= e^{2\pi i \frac{\sqrt{f^2+x^2}}{\lambda}} \quad (19)$$

Equation 19 can be filled into equation 9.

$$U_2(x') = -\frac{1}{2\pi} \iint_S e^{-ik\sqrt{f^2+x^2}} \left(ik - \frac{1}{r} \right) \frac{e^{ikr} \cos(\theta)}{r} dx dy \quad (20)$$

$$= -\frac{1}{2\pi} \iint_S \left(ik - \frac{1}{r} \right) \frac{e^{ik(r-\sqrt{f^2+x^2})} \cos(\theta)}{r} dx dy \quad (21)$$

As $r \geq f$ and for 3D it was concluded in appendix B that $fk \gg 1$, the $\frac{1}{r}$ term can be neglected.

$$U_2(x') = -\frac{ik}{2\pi} \iint_S \frac{e^{ik(r-\sqrt{f^2+x^2})} \cos(\theta)}{r} dx dy \quad (22)$$

This integral cannot be calculated analytically. The numerical solution for the intensity $I_f(x') = |U_2(x')|^2$ is given in Figure 1.5a. The maximal value is $|U_2(0)| = 4.58$ and thus $I_f(0) = 20.99$.

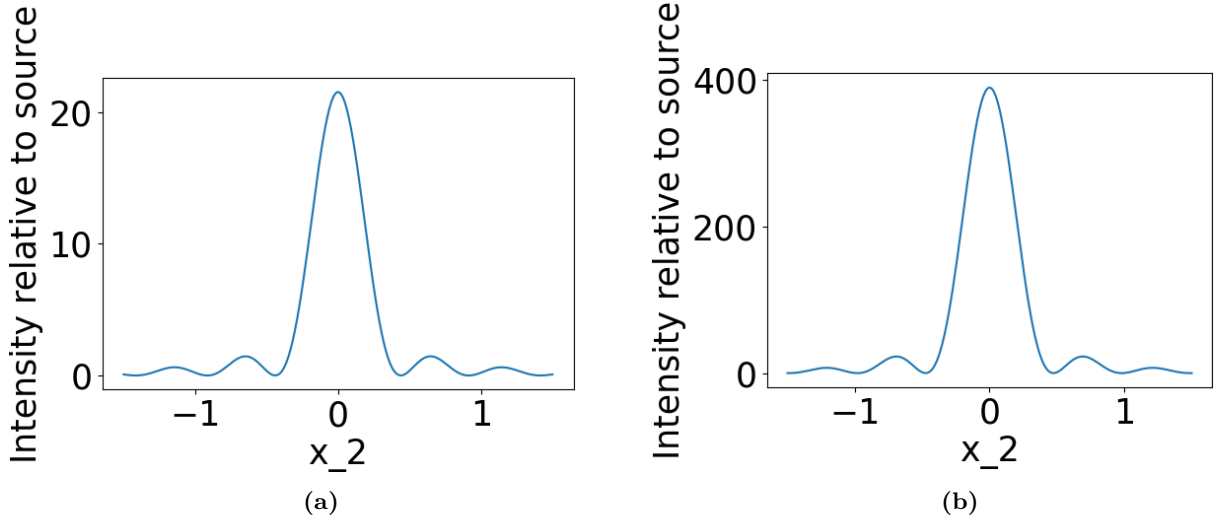


Figure 1.5: The intensity at the focal line/plane for a (a) 2D and (b) 3D lens. The maximum relative intensity is $I_f(0) = 20.99$ for the 2D lens and $I_f(0,0) = 389.96$ for the 3D lens, while the first zero is at $x = 0.44$ μm for the 2D lens and at $x = 0.474$ μm for the 3D lens. Finally, the full-width at half-max (FWHM) is 0.402 μm for the 2D lens and 0.424 μm for the 3D lens. Mind the different scale for the two figures.

Although the intensity profile in Figures 1.5a and 1.5b might look like a sinc and a Bessel function respectively, this is not the case. These simplified formulas are only obtained with the Fresnel approximation, which gives a relative error of 30 %. The Fresnel derivation and the reason why it is not sufficient are given for 2D in appendix A.

1.3 Direct design of metasurfaces

The previous section gave more insight in the working principle of a lens, derived the optimal linear transformation of the fields due to the lens and quantified the maximal intensities that can be achieved. This section builds further on these results to design metasurfaces.

1.3.1 Phase modulation in practice

As discussed in the previous section, an ultra-thin metasurface can be seen as a linear transformation of the field.

$$U_1 = \mathcal{T}_1(U_0) \quad (23)$$

Assuming the lens is non-absorbing and non-reflective, the linear transformation \mathcal{T}_1 can only change the phase and must conserve the modulus of U_0 . The previous section discussed the optimal linear transformation for two applications: a lens and a frequency splitter. However, in reality, the optimal linear transformation cannot be achieved exactly, due to a lack of degrees of freedom. In addition to considering the figure of merit of the metasurface, manufacturability and cost must be taken into account.

To easily integrate the metasurfaces in electronics, only silicon oxide (SiO_2) and titanium oxide (TiO_2) are used to construct the lenses. Additionally, only planar structures that can be made by subsequent oxide depositions and lithography are considered. Figure 1.6 gives an example of such a structure. The light gray indicates SiO_2 and the black indicates TiO_2 . In this example, the structure consists of two layers on top of each other. Additionally, a minimum feature size of 90 nm is used. This means that the width of a certain feature (SiO_2 between TiO_2 or vice versa) cannot be smaller than 90 nm. The minimum feature size will often be visualised by a blue dot with diameter equal to the minimum feature size, as can be seen on Figure 1.6 as well.



Figure 1.6: Example of a manufacturable metasurface with a minimum feature size of 90 nm.
Light gray: SiO_2 and black: TiO_2 .

At least two materials are needed to modulate the phase of the incoming wave. The principle is given in Figure 1.7. A plane wave comes from a SiO_2 block (light gray). The incoming wave is completely in phase. Then the wave passes through the metasurface which consists partly of SiO_2 with refractive index $n_{\text{SiO}_2} = 1.45$ and partly of TiO_2 (black) with refractive index $n_{\text{TiO}_2} = 2.7$ (Polyanskiy, n.d.). Due to a difference in refractive index the wavelength of the light wave is different and, depending on the thickness of the metasurface, the phase after the metasurface is different. Choosing specific thicknesses and specific materials allows to modulate the phase and thus design a structure that resembles as close as possible the linear transformation \mathcal{T}_1 discussed in the previous section.

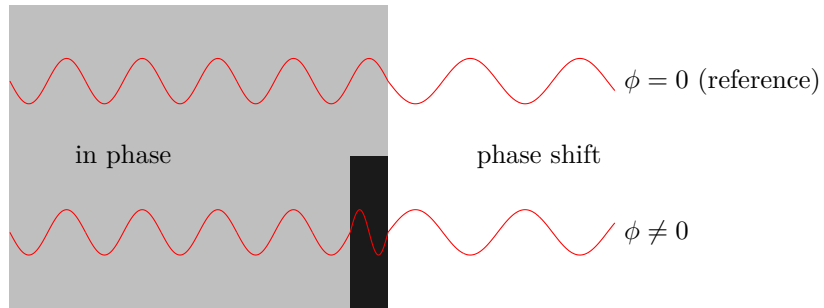


Figure 1.7: Illustration of the modulation of the phase by a metasurface with SiO_2 (light gray) and TiO_2 (black) in an environment of air (white).

However, due to manufacturing constraints it is impossible to match the optimal phase transformation perfectly. Only two materials are used and the layers have a uniform thickness over the lateral dimensions. So, if there is only one layer, only two different phases are possible: either the reference phase after a SiO_2 -part or the phase shift induced by a TiO_2 -part. More degrees of freedom can be achieved by adding more layers, however this requires more lithography steps and therefore makes it more expensive and creates challenges regarding the alignment of the layers.

1.3.2 Direct design of a lens

The next paragraphs describe how to match the optimal phase transformation as close as possible. First, the case that there is only one frequency is discussed. In section 1.3.3 the theory will be generalised to multiple frequencies.

The first parameter that needs to be determined is the layer thickness. In general for all applications, the phase shift needs to be modulated as precisely as possible. However, as mentioned in the previous paragraph, if there is only one layer, only two different phases are possible: either the reference phase after SiO_2 or the phase after TiO_2 . It's trivial that for optimal control of the phase, the feasible phases should be distributed as equally as possible over the unit circle ($[0, 2\pi]$). Thus, if there is only one layer, making only two distinct phases feasible, these phases should equal 0 and π . Every phase in $\phi \in [-\pi/2, \pi/2]$ can then be approximated by $\phi = 0$ and every phase in $\phi \in [\pi/2, 3\pi/2]$ can then be approximated by $\phi = \pi$. This is illustrated in Figure 1.8.

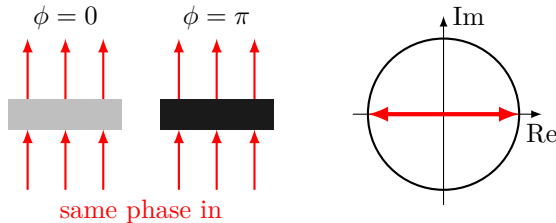


Figure 1.8: Representation of the required phases to achieve optimal control.

To achieve a phase shift of π , the difference in the effective distance (distance multiplied by refractive index nd) should be equal to half a wavelength.

$$(n_2 - n_1)d = \frac{1}{2}\lambda(2m + 1) \quad m \in \mathbb{N} \quad (24)$$

With n_i the refractive index of material i , d the thickness of the layer, λ the wavelength and m a natural number. In most applications, the metasurface should be as thin as possible, so m can be chosen to be equal to 0. Equation 24 determines the optimal thickness d for the layer. For example, if the wavelength is $\lambda = 600 \text{ nm}$, the refractive indices are $n_1 = 1.45$ for SiO_2 and $n_2 = 2.7$ for TiO_2 and m is set to 0, then $d = \frac{\lambda}{2(n_2 - n_1)} = 240 \text{ nm}$.

The more layers there are, the more degrees of freedom are available. Two different cases are discussed: the first case requires that all layers have the same thickness, while the second case assumes that every layer can be optimised separately. The former will be called "uniform thicknesses" as the layer thicknesses are uniform, i.e they are all the same. The latter will be called "exponential thicknesses", for reasons that will become clear later. Only the total TiO_2 thickness is assumed to be relevant to determine the phase, all reflections in between layers are neglected. Thus the order of the layers is unimportant in the theory that will be developed in the next paragraphs.

For the uniform thicknesses, it does not matter which layers are "on"², it only matters how many layers are "on", as all layers have the same thickness. So for X layers, there are $X + 1$ feasible phases, i.e the phase when 0 layers, 1 layer, ..., $X - 1$ layers or X layers are on. Thus there are $X + 1$ different phases that need to be distributed equally over the interval $[0, 2\pi]$. As a result, the optimal phases are given by

$$\phi_k = 2\pi \frac{k}{X + 1}, \quad \text{with } k = 0, 1, \dots, X \quad (25)$$

With k the amount of layers that are on, X the total amount of layers and ϕ_k the phase corresponding to that configuration. From equation 25 it is clear that the thickness of a single layer needs to induce a phase shift of $\frac{2\pi}{X+1}$, thereby the thickness of every layer follows from the following modified Bragg equation.

$$(n_2 - n_1)d = \frac{1}{X + 1}\lambda(2m + 1) \quad m \in \mathbb{N} \quad (26)$$

²A part that is TiO_2 is considered to be "on", while a part that is SiO_2 is considered to be "off"

It is clear that equation 26 reduces to equation 24 for $X = 1$, this should be the case, as one layer always has a uniform thickness over all layers. In the case that the wavelength is $\lambda = 600$ nm, the refractive indices are $n_1 = 1.45$ for SiO_2 and $n_2 = 2.7$ for TiO_2 and m is set to 0, then $d = \frac{\lambda}{3(n_2 - n_1)} = 160$ nm for $X = 2$, $d = \frac{\lambda}{4(n_2 - n_1)} = 120$ nm for $X = 3$, etc. The layers and the feasible phases are visualised for two and three layers in Figure 1.9.

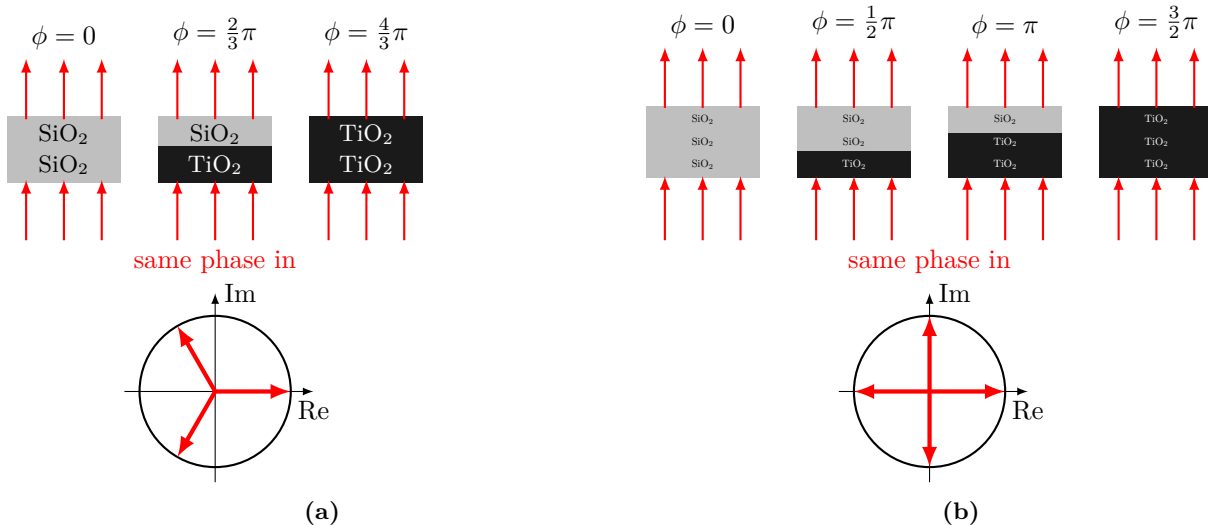


Figure 1.9: Representation of the required phases to achieve optimal control for uniform thicknesses for (a) two layers and (b) three layers.

The disadvantage of the strategy used above, is that there are equivalent configurations giving rise to the same phase shift. For example, the middle configuration in Figure 1.9a with the bottom layer on and the top layer off, would be equivalent to a configuration with the top layer on and the bottom layer off. In fact, for X layers, there should be 2^X possible combinations, whereas for the uniform thicknesses only $X + 1$ different phases are feasible. The problem statement to get as much information from certain "on" or "off" combinations is well known in information theory and solved by binary coding. In a binary number, the digits have a value that decreases exponentially with a factor two. For example $(100)_2$ is equal to four, while $(010)_2$ is only equal to two and $(001)_2$ represents one. Although only three digits are used, eight different numbers can be represented that are equally spaced (the integers from 0 to 7). A similar strategy can be used to design a metasurface, namely the most phases can be made feasible by having layers that increase exponentially in thickness, hence exponential thicknesses. As a result, for X layers, the following phases are possible:

$$\phi_k = 2\pi \cdot \frac{k}{2^X}, \quad \text{with } k = 0, 1, \dots, 2^X - 1 \quad (27)$$

All these phases are possible if the layers have the following thicknesses d_k :

$$(n_2 - n_1)d_k = 2^{-k}\lambda(2m+1) \quad k = 1, 2, \dots, 2^X; m \in \mathbb{N} \quad (28)$$

Again, it is clear that equation 28 reduces to equation 24 for $X = 1$. In the case that the wavelength is $\lambda = 600$ nm, the refractive indices are $n_1 = 1.45$ for SiO_2 and $n_2 = 2.7$ for TiO_2 and m is set to 0, then for $X = 2$: $d_1 = \frac{\lambda}{2(n_2-n_1)} = 240$ nm and $d_2 = \frac{\lambda}{4(n_2-n_1)} = 120$, while for $X = 3$: $d_1 = \frac{\lambda}{2(n_2-n_1)} = 240$ nm, $d_2 = \frac{\lambda}{4(n_2-n_1)} = 120$ and $d_3 = \frac{\lambda}{8(n_2-n_1)} = 60$, etc. The layers and the feasible phases are visualised for two and three layers in Figure 1.10.

Once the thicknesses are determined and the optimal phase shift is known from the mathematical model in section 1.2, the direct design is trivial. The feasible phase shifts are known, so every phase must be rounded to the nearest feasible phase. It must be noted that the off-set of the phase is not important, only the relative differences are important, thus there remains one free parameter. This parameter can be optimised by minimising the root-mean-square error of the phase. Figure 1.11a shows an example of a direct designed lens and the desired phase calculated in section 1.2 plotted on top. The lens only has one layer, so only two phases are feasible. All

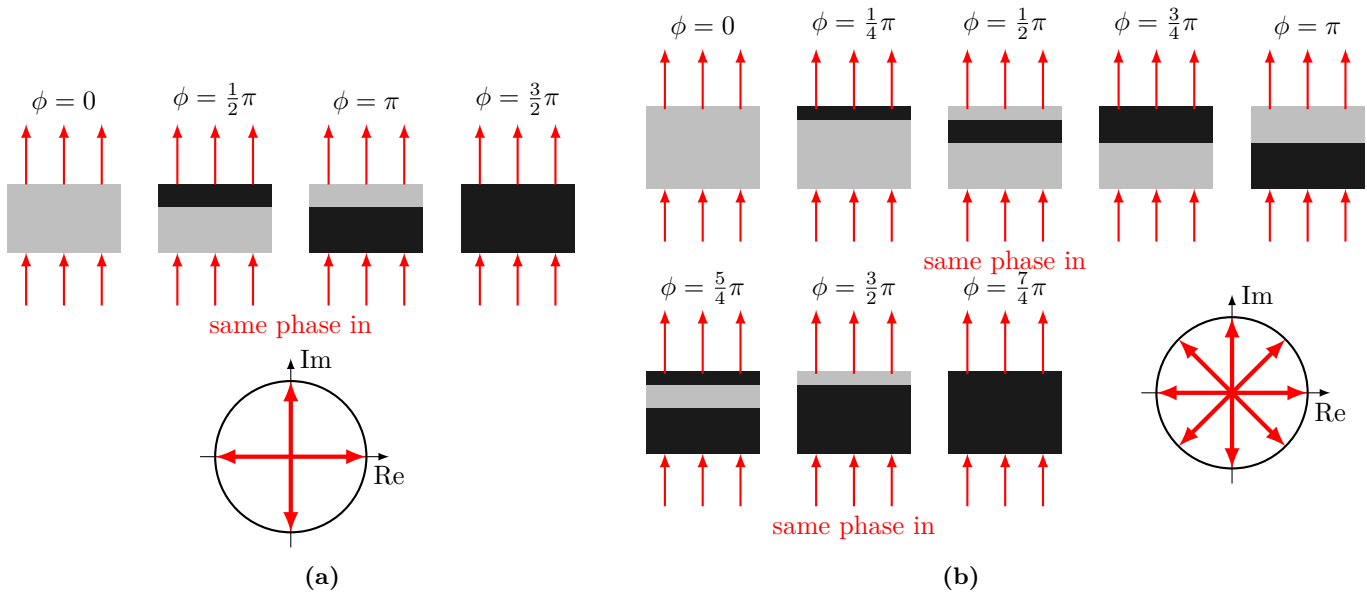


Figure 1.10: Representation of the required phases to achieve optimal control for exponential thicknesses for (a) two layers and (b) three layers. SiO₂ is colored light gray and TiO₂ is colored black.

positions where a phase $\phi \in [0, \pi]$ is needed, are made in SiO_2 , while all positions where a phase $\phi \in [\pi, 2\pi]$ is needed, are made in TiO_2 . Figure 1.11b shows an inverse designed lens, using the adjoint method in Meep as described in section 1.4. The Figure shows how closely the inverse design resembles a direct design. There are two layers with exponential thicknesses, so there are four feasible phases. That's why the unit circle is divided into four equal parts: red-to-yellow $\phi \in [0.14, 0.39] \cdot 2\pi$, yellow-to-blue $\phi \in [0.39, 0.64] \cdot 2\pi$, blue-to-black $\phi \in [0.64, 0.89] \cdot 2\pi$ and black-to-red $\phi \in [0.89, 1.14] \cdot 2\pi$. Every part corresponds to a specific combination of layers being on or off. The inverse design resembles the direct design very well. The fact that the adjoint solver of Meep comes up with a design predicted by the direct design, confirms the validity of the theory presented above. However, Meep can improve the design slightly by taking into account the finite thickness of the lens, and by producing small features to turn on a layer only partly and reach phases in between the feasible phases discussed above.

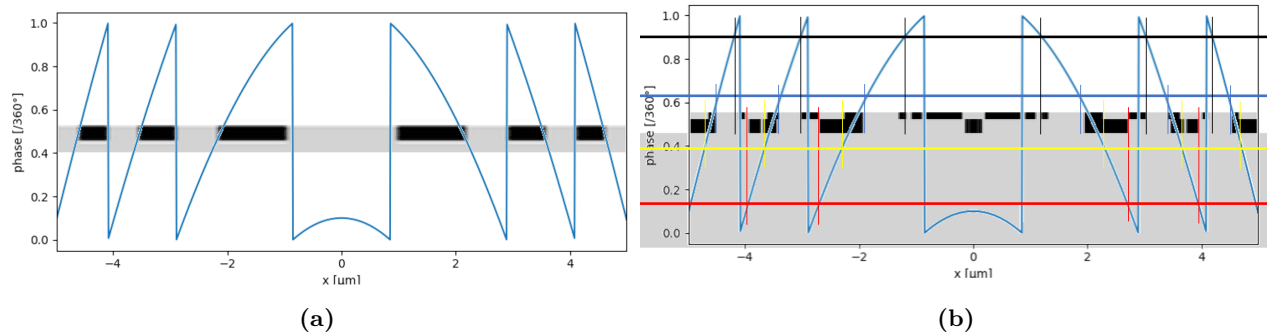


Figure 1.11: (a) method to design a lens and (b) comparison between direct design and inverse design. SiO_2 is colored light gray and TiO_2 is colored black.

1.3.3 Direct design of a frequency splitter

In this section, the more general case with multiple frequencies where each frequency requires a different linear transformation is discussed. To simplify notation, the frequency vector $\vec{\phi}$ is defined, whose elements are the phases of the frequencies. The required frequency shifts are given in equation 8. Figure 1.12 plots an example of

the required phase vectors for an optimal frequency splitter. As can be seen on Figure 1.12b, the phase vector can take almost any value in \mathbb{R}^2 and thus as many phases as possible in \mathbb{R}^2 should be feasible.

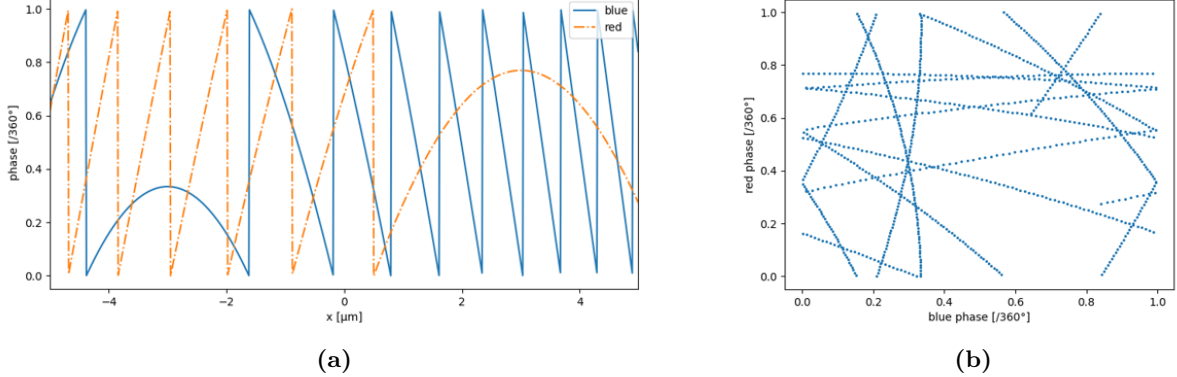


Figure 1.12: The required phases for a non-periodic 2D frequency splitter of red (650 nm) and blue light (470 nm) with width $w = 10 \mu\text{m}$, focal points at a distance $f = 6 \mu\text{m}$ and both 3 μm off-axis. (a) the phase in function of the distance and (b) the values that the phase vector $\vec{\phi} = (\phi_{\text{blue}}, \phi_{\text{red}})$ takes.

Similarly as in the previous section, the optimal phase vector can never be achieved exactly at every position, due to manufacture constraints. This section investigates how the optimal phase vector can be approximated as closely as possible. Also in this case, the layer thicknesses determine which phase vectors are feasible. Particularly, the phase vector is determined by the total TiO_2 thickness:

$$\vec{\phi} = 2\pi(n_{\text{TiO}_2} - n_{\text{SiO}_2})d_{\text{TiO}_2}\vec{\lambda}^{-1} \bmod 2\pi \quad (29)$$

Where $\vec{\phi} = \begin{bmatrix} \phi_1 \\ \vdots \\ \phi_m \end{bmatrix}$ is the phase vector, d_{TiO_2} is the total thickness that is "on" and can take maximally 2^X different values if none of the thicknesses is a discrete linear combination of the other thicknesses. $\vec{\lambda}^{-1} = \begin{bmatrix} 1/\lambda_1 \\ \vdots \\ 1/\lambda_m \end{bmatrix}$

is the vector containing the reverse of all the wavelengths that need to be split. In the right hand side of equation 29, everything is fixed, except for the TiO_2 thickness. Hence to enable a flexible design, the thicknesses should be optimised in such a way that the set of feasible phase vectors spans \mathbb{R}^m as well as possible, with m the number of frequencies. The problem statement to determine the optimal thicknesses is visualised in Figure 1.13 for the specific case of four layers and two frequencies. From four thicknesses the $2^4 = 16$ feasible phase vectors can be computed using equation 29. The Figure of merit is defined as the root means square (RMS) of the distance to the closest feasible phase vector.

$$FOM = \iint_S \min_i \left(|\vec{\psi} - \vec{\phi}_i|^2 \right) d\vec{\psi} \quad (30)$$

This optimization problem cannot be solved analytically, but a Metropolis Monte Carlo algorithm was implemented. The code for this algorithm can be found in appendix E.

Equation 30 can be easily generalised to m frequencies by using an m -dimensional integral.

$$FOM = \iint \dots \int_{[0,2\pi]^m} \min_i \left(|\vec{\psi} - \vec{\phi}_i|^2 \right) d\vec{\psi} \quad (31)$$

However, the more frequencies, the more computationally demanding the integral is and thus to harder to optimize the thicknesses as many of these integrals need to be calculated during the optimization. That's why

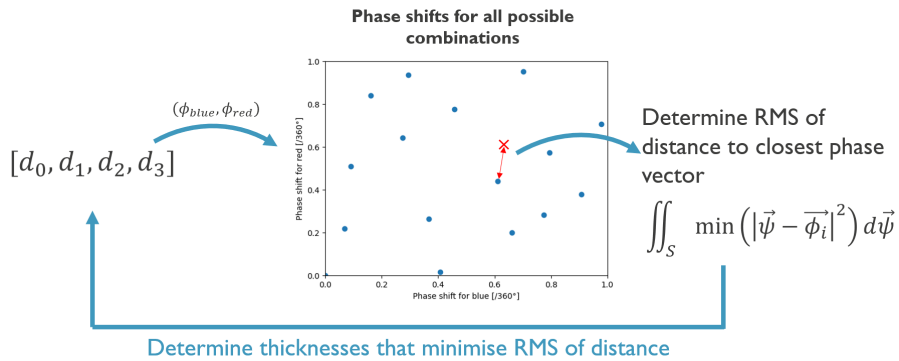


Figure 1.13: Schematic of the problem statement to determine the optimal thicknesses for four layers and two frequencies.

the code provided in appendix E uses Monte Carlo integration, which scales better to higher dimensions than regular deterministic integration methods.

Once the thicknesses are determined, the frequency splitter can be designed by calculating the required phase vector at every position as in Figure 1.12 and then picking the combination of layers whose phase vector is as close as possible to the required phase vector. No direct design was made, however the optimal thicknesses were used in the inverse design, as described in section 3.

1.4 Inverse design

This section presents inverse design, and the method used to conduct it. Let us consider a certain structure with a defined geometry. Calculating the resulting electric and magnetic fields through this source is a well-documented process in which Maxwell's equations are solved using various methods such as finite-difference time-domain (FDTD, see section 1.5.1). However, one can be interested in the opposite problem: *which structure can produce a desired electromagnetic response?* (Miller, 2012). Electromagnetic inverse design is a part of the

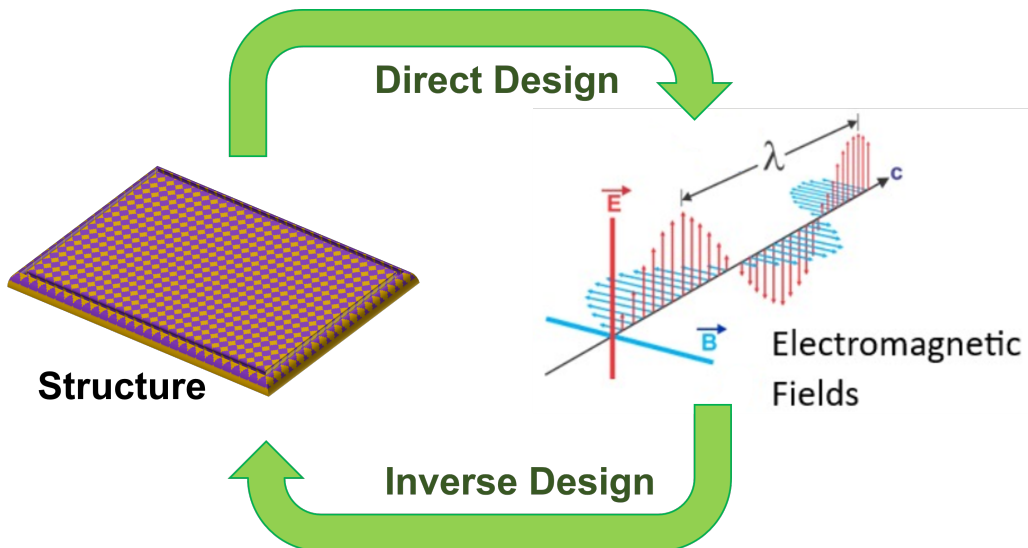


Figure 1.14: Inverse design methodology.

larger category of optimization problems known as topology optimization which consist in finding a structure which minimizes an objective function F , while being subject to a number of constraints G_i . This problem can

be written as:

$$\begin{cases} \min : & F(\mathbf{u}(\rho), \rho) \\ s.t. & G_0(\rho) = \int_{\Omega} \rho dV - V_0 \leq 0 \text{ (Volume constraint)} \\ & G_i(\mathbf{u}(\rho), \rho) \leq 0 \text{ for } j = 1, \dots, m \\ & \rho(x) = 0 \text{ or } 1 \forall x \in \Omega \end{cases} \quad (32)$$

where $\rho(\mathbf{x})$ describes the material distribution of volume Ω and $\mathbf{u}(\rho)$ a state field (Sigmund and Maute, 2013). In the case of electromagnetic topology optimization, the objective F is the intensity of the field at a desired point, subject to the four Maxwell equations:

$$\begin{cases} \text{maximize} & F(\vec{E}, \vec{H}, \omega) \\ s.t. & \nabla \cdot \bar{\epsilon} \vec{E} = \rho \\ & \nabla \cdot \bar{\mu} \vec{H} = 0 \\ & \nabla \times \vec{E} = -j\omega \bar{\mu} \vec{H} \\ & \nabla \times \vec{H} = \vec{J} + j\omega \bar{\epsilon} \vec{E} \end{cases} \quad (33)$$

where the objective is to find the permittivity tensor $\bar{\epsilon}$ and permeability tensor $\bar{\mu}$ that maximize the value of the objective function.

For the problems described hereunder, the objective function was chosen to be the intensity of one of the electric field's components at the focal point:

$$F = |\vec{E}(\vec{r}_0)|^2 \quad (34)$$

For 2D simulations, the chosen component was E_z and for 3D simulations, E_x was selected, although E_y can be used as well, or a combination of the last two. $\epsilon(\vec{r})$ is denoted as the design parameters to avoid confusion with the electric charge density.

1.4.1 Adjoint method

The adjoint method is an optimization technique used to optimize complex structures. It works by introducing the adjoint electromagnetic field, auxiliary to the direct field. Whereas the direct field is calculated by propagating the electromagnetic field through a structure, the adjoint field is obtained by propagating the desired field backwards through the structure, as in Figure 1.15 (Miller, 2012; Molesky, Lin, Piggott, et al., 2018). The field of interest for the applications presented in this report are the electric fields \mathbf{E} therefore we will solve for them. The adjoint fields are denoted by \mathbf{A} .

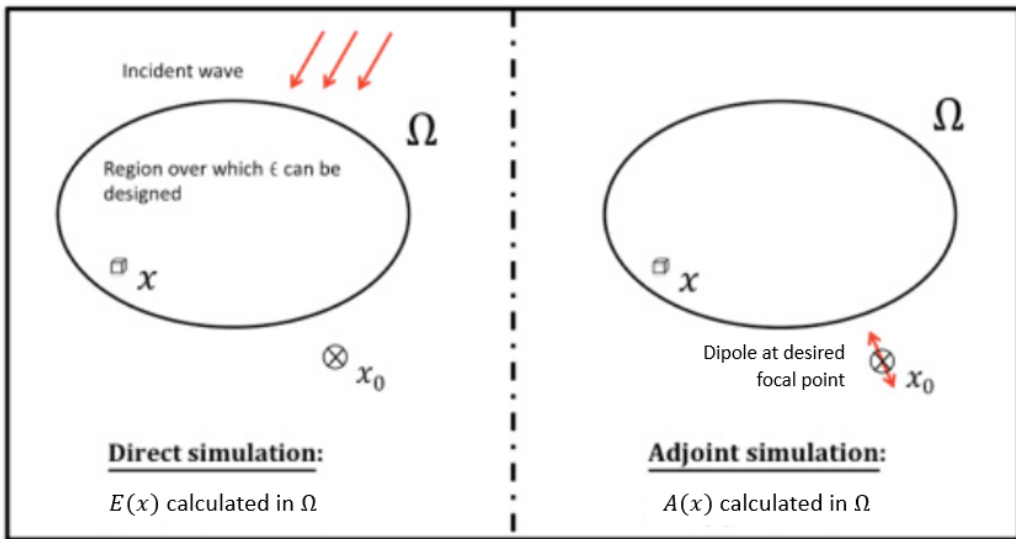


Figure 1.15: Schematic of direct and adjoint simulation runs (Lalau-Keraly et al., 2013).

Using Lorentz's reciprocity principle for electromagnetism, the gradient of the objective function is calculated using both direct and adjoint fields. For a small volume dV having permittivity $\Delta\epsilon_r$, the (Lalau-Keraly et al., 2013):

$$\frac{\Delta F}{\Delta\epsilon_r} = \text{Re} [\vec{\mathbf{A}} \cdot \vec{\mathbf{E}}] \quad (35)$$

Using the value for F calculated in the direct run, the direct and adjoint electric fields, the gradient of ϵ_r can be obtained and optimized using a gradient descent method. When applied iteratively, this method will lead to an optimum. The permittivity function $\epsilon_r(\mathbf{x})$ describes the material structure, and maps each point to a value between 0 and 1 corresponding to two materials with permittivities ϵ_{r1} and ϵ_{r2} .

To ensure metasurface manufacturability, each point must have a single, well defined material (there cannot be a point with a value halfway between the two materials). It therefore needs to undergo binarization as the solver converges towards the optimal structure. This is done by adding a new thresholding parameter β which is increased every few iterations, and which modifies the structure according to the "hat filter", in equation 36 (Hammond et al., 2022). The value of this function for different values of β can be found in Figure 1.16. The parameter η corresponds to the mapping threshold.

$$P(x) = \frac{\tanh(\beta\eta) + \tanh(\beta(x - \eta))}{\tanh(\beta\eta) + \tanh(\beta(1 - \eta))} \quad (36)$$

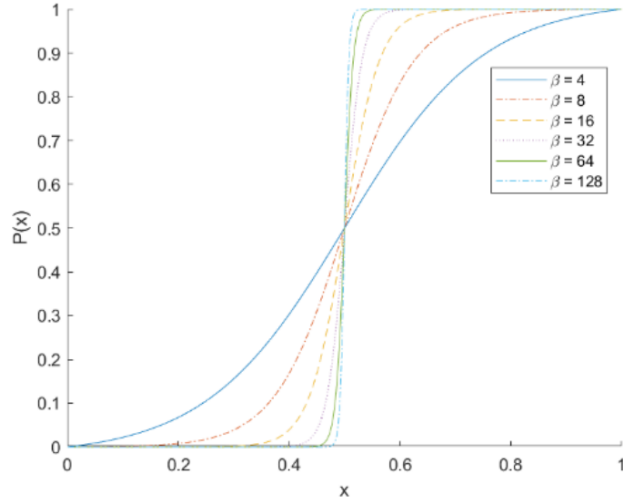


Figure 1.16: Hat filter $P(x)$ for different values of β .

The optimization process is as follows (Hammond et al., 2022): first the structure undergoes filtering and projection. Then, a direct or forward run is executed to evaluate the value of the objective function F . Third, an adjoint run is executed from the desired sources, in that case a point source from each desired focal point. Finally, the gradient of the objective function is calculated for use by an optimization algorithm (in this case, the method of moving asymptotes, see Svanberg, 2002).

This process is conducted iteratively with an increasing binarization, until a certain tolerance is reached (the structure has reached convergence) or the solver has reached the maximum number of iterations, defined by the user.

1.5 Simulation

1.5.1 Finite Difference Time Domain (FDTD) Method

The electromagnetic FDTD algorithm is a numerical simulation method for solving directly the Maxwell's time-dependent curl equations or their equivalent integral equations using the finite difference technique. The FDTD method was introduced for the first time in 1966 by Kane S. Yee and has been perfected throughout time by

researchers in electromagnetics. It is classified as a grid-based differential time domain numerical modeling method and its solutions have the advantage of covering a wide range of frequencies with a single simulation run (Narayan et al., 2017). The method involves dividing space and time into a discrete grid and updating the electric and magnetic fields at each point of the grid based on their values at neighboring points, as well as the local sources of those fields (Yee, 1966). The increments in space and time have to be selected in a way that avoid aliasing of the continuous field distribution and guarantee the stability of the time-marching algorithm.

1. Maxwell's Curl Equations: The differential time domain Maxwell's equations in a linear isotropic and frequency-independent medium can be written as six coupled scalar equations that make up the building block for the FDTD algorithm (Narayan et al., 2017):

$$\frac{\partial H_x}{\partial t} = \frac{1}{\mu} \left[\frac{\partial E_y}{\partial z} - \frac{\partial E_z}{\partial y} - \delta H_x \right] \quad (37)$$

$$\frac{\partial H_y}{\partial t} = \frac{1}{\mu} \left[\frac{\partial E_z}{\partial x} - \frac{\partial E_x}{\partial z} - \delta H_y \right] \quad (38)$$

$$\frac{\partial H_z}{\partial t} = \frac{1}{\mu} \left[\frac{\partial E_x}{\partial z} - \frac{\partial E_z}{\partial x} - \delta H_z \right] \quad (39)$$

$$\frac{\partial E_x}{\partial t} = \frac{1}{\varepsilon} \left[\frac{\partial H_z}{\partial y} - \frac{\partial H_y}{\partial z} - \sigma_e E_x \right] \quad (40)$$

$$\frac{\partial E_y}{\partial t} = \frac{1}{\varepsilon} \left[\frac{\partial H_x}{\partial z} - \frac{\partial H_z}{\partial x} - \sigma_e E_y \right] \quad (41)$$

$$\frac{\partial E_z}{\partial t} = \frac{1}{\varepsilon} \left[\frac{\partial H_y}{\partial x} - \frac{\partial H_x}{\partial y} - \sigma_e E_z \right] \quad (42)$$

where: E_i is the component of the electric field in the i direction, H_i is the component of the magnetic field in the i direction, ε is the electric permittivity, σ_e is the electric conductivity, μ is the magnetic permeability and δ is the magnetic resistivity.

2. Yee's FDTD Algorithm: This algorithm uses second-order central differences. Its main steps are described below:

- (a) Discretize space and time: Use finite differences to replace the derivatives in the Ampere's and Faraday's laws.
- (b) Solve the difference equations: This way the future fields will be expressed in terms of the past fields.
- (c) Evaluate the magnetic fields one time step in the future.
- (d) Evaluate the electric fields one time step in the future.
- (e) The evaluation of the magnetic and electric field have to be repeated until reaching the desired duration (Narayan et al., 2017).

The Yee FDTD algorithm uses the grid shown in Figure 1.17, where the \vec{E} and the \vec{H} components are arranged in such a way that every \vec{E} component is surrounded by four \vec{H} components and vice versa.

3. Implementation of FDTD Method: To apply the FDTD method, it is necessary to establish a physical region for the simulation or computational domain. Then, the materials should be specified, followed by the source. The selection of the cell size is a compromise between getting accurate results (small cell size) and lower computational cost (large cell size). But, most importantly, the cell size have to be smaller than the smallest wavelength for which accurate results are desired, a rule of thumb is to make the cell size ten times smaller than the smallest wavelength to achieve accurate results. Afterwards, the time step is determined to insure the stability of the time-stepping algorithm. Finally, the boundary conditions are set. Berenger's perfectly matched layer (PML) is an example of boundary conditions, where the fields are damped as they propagate into the absorbing medium (Narayan et al., 2017).

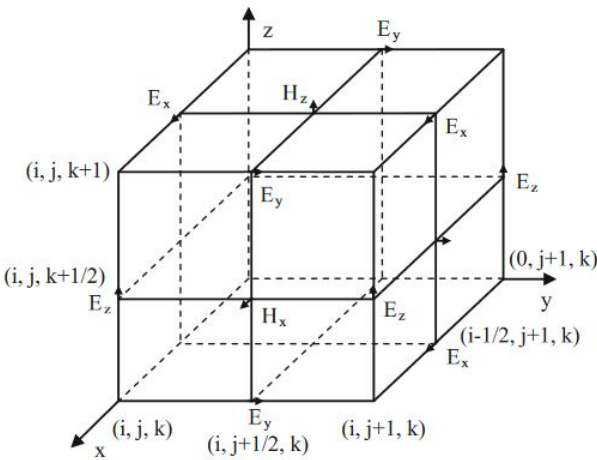


Figure 1.17: Yee cell geometry (Narayan et al., 2017).

1.5.2 MEEP

The program used for this project is MEEP, an open-source FDTD solver developed at MIT which also implements the adjoint method for inverse design (Hammond et al., 2022; Oskooi et al., 2010). The program was run through its Python interface.

Unlike other FDTD software packages, MEEP allows a more flexible access to the source code. MEEP is also a full-featured package, that includes different media, boundary conditions, and coordinate systems. But, additionally, it offers unusual features, such as advanced signal processing, accurate subpixel averaging, a frequency domain solver, among others (Oskooi et al., 2010).

1.5.3 Far Fields

Near-to-far-field transformation on the frequency domain can be computed by Meep when providing the fields on a "near" bounding surface within the simulation cell. Meep computes the fields at arbitrarily distant points using an analytical transformation assuming that the "near" surface and the "far" region exist within a single homogeneous non-periodic 2D, 3D, or cylindrical region. In simulations enclosed by Perfectly Matched Layers (PML) that absorb outgoing waves, the near-to-far-field feature allows the computation of fields outside the cell as if the absorbed waves were still present, essentially in an infinite open volume ("MEEP Documentation", n.d.).

This operation is performed on Fourier-transformed fields. By specifying a set of desired frequencies, Meep accumulates the Fourier transforms and then computes the fields at each frequency for the designated far-field locations. The process relies on the principle of equivalence, where Meep calculates equivalent currents based on the Fourier-transformed tangential fields on the "near" surface and convolves them with analytical Green's functions to determine the fields at any desired point within the "far" region ("MEEP Documentation", n.d.).

The three steps of the near-to-far-field feature are:

1. Define the "near" surface(s) as a collection of surfaces that capture all outgoing radiation in the desired directions.
2. Run the simulation to accumulate the Fourier transforms on the "near" surface(s).
3. Compute the far fields at any desired point in space.

1.5.4 Exploiting parallelism

As FDTD problems grow in size and time, they can become very computationally expensive, especially when dealing with three-dimensional spaces. MEEP enables its users to divide their simulations in multiple processes and run them in parallel on multi-core machines, while communicating between themselves using MPI, a protocol for inter-process communication (Oskooi et al., 2010). This is achieved through three different methods:

- Spatial parallelism, which involves dividing the simulation region into multiple subregions, each assigned to a different processor core which, at each timestep, updates the fields at every voxel and communicates the fields on its exterior surfaces to neighboring chunks.
- Frequency parallelism, which involves computing gradients for multiple frequencies simultaneously.
- Simulation parallelism, where gradients for different design fields or objective functions are divided among different processor groups.

By leveraging these three techniques on multi-core machines possessing up to 64 CPU cores, the simulation times have been greatly reduced from several weeks to a few hours or days.

2 Focusing lens

Metalenses have been gaining popularity due to their ability to mimic traditional optical components while being significantly smaller in size and also providing novel functionalities. They enable the production of lenses with greater NA, that can be easily integrated in CMOS technology, that can have different functionalities depending on frequency or polarization, etc. (Arbabi and Faraon, 2023). In this section a broadband (550 nm to 650 nm) focusing lens is implemented as a metasurface. The theory of a focusing metalens is discussed in sections 1.2 and 1.3. A conventional lens might not seem very impressive, however it forms the basis of more complicated elements like a frequency splitter and a retroreflector discussed in the following sections. This section starts by giving the problem statement, it then elaborates on the optimization algorithm used and finally gives an overview of the most important results.

2.1 Problem Statement

Section 1.3.2 discussed how a lens can be designed purely from a theoretic point of view. However, a few approximations were made, namely that the lens is infinitely thin, there is no reflection on material boundaries and only the "feasible phases" can be achieved behind the lens. By using FDTD simulations, the intensity at the focal point can be calculated taking into account all these effects. Then the adjoint method can be used to compute the gradient and finally an optimization algorithm can find the optimal structure, as discussed in section 1.4.1. This structure will resemble the direct design if the approximations made are sufficiently small. However, because these effects are taken into account, the numerical optimization should be able to come up with an even better design. Therefore the aim of this section is partly to design better lenses than the direct design and partly to confirm the mathematical model used in the direct design, presented in section 1.2.

Often the disadvantage of metasurfaces is that they are designed for one specific wavelength. However, in this section a broadband lens is designed that optimizes the focusing of light with wavelength 550 nm, 600 nm and 650 nm at the same time. The lens has a width $w = 10 \mu\text{m}$ and is integrated in SiO_2 . The thicknesses of the layers are determined by the method described in section 1.3.2 implemented for the center wavelength of 600 nm. An example of such a structure is given in Figure 2.1. The lens is mounted on a SiO_2 slab (black) and focuses the light in air (white). The example has two layers with exponential thicknesses (black hatched blue), the thicknesses are not optimized by Meep. The light source is placed directly below the lens (red line) and emits E_z (TE) polarised light at the three frequencies. The boundaries of the cell incorporate perfectly matched layers (PMLs; hatched green), they absorb the incoming light and reflect nothing. The simulation is not extended to the focal point, instead a monitor is placed right above the lens (blue line) which measures the fields and calculates the intensity at the focal point using the near-to-far transformation implemented in Meep, explained in section 1.5.3 (Oskooi et al., 2010). The average intensity at the focal points for the three frequencies is then maximized using the adjoint solver implemented in Meep as discussed in section 1.4.1 (Hammond et al., 2022).

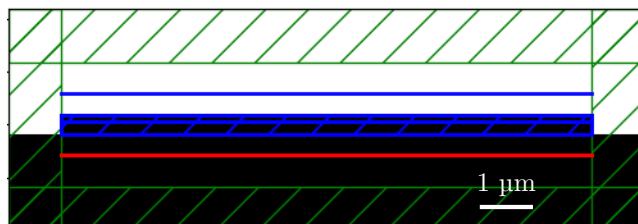


Figure 2.1: Structure implemented in Meep.

The adjoint solver allows to specify a minimum feature size (MFS) that puts a limit to the width of a TiO_2 part in SiO_2 and vice versa. This is essential to allow the production of the structures. Most designs discussed in this section have a MFS of 90 nm, unless specified otherwise. Some experiments have the aim of verifying the physical limits discussed in section 1.2 and have therefore a MFS of only 10 nm.

The structure of the 3D metalens is exactly the same, only the lens is now a square of 10 μm by 10 μm and only one wavelength (600 nm) is used to speed up the computationally expensive 3D calculations.

2.2 Optimization algorithm

The structures are optimized using the adjoint method, discussed in section 1.4.1. The adjoint method enables an inexpensive calculation of the gradient. When the gradient is known, the structure can be optimized using a gradient optimization algorithm. It was decided to use the method of moving asymptotes, implemented in the nlopt package (Johnson, 2014; Svanberg, 2002). A problem that often occurs with gradient optimization is that the algorithm gets stuck in local minima, which results in suboptimal structures. To anticipate on this problem, two potential solutions were tested.

The first approach is referred to as random sampling. This simply means that multiple random starting conditions are chosen and the structure is optimized from all of these starting conditions. In the end, the structure that reaches the best figure of merit, i.e. the highest intensity at the focal point is the optimal structure. This algorithm is visualised in Figure 2.2.

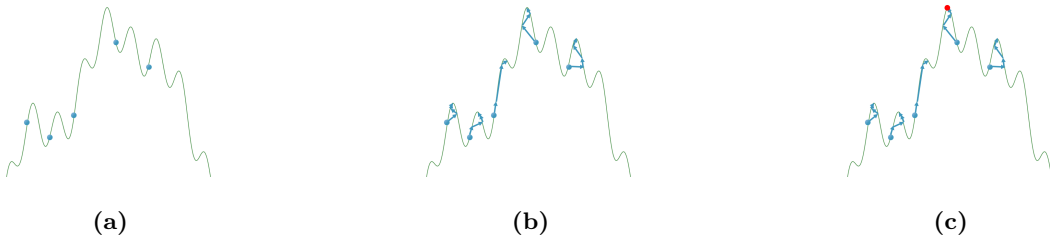


Figure 2.2: Random sampling optimization: (a) a number of random samples are chosen, (b) all samples are optimized locally and (c) the best optimized sample is the optimal structure.

Figure 2.3 shows a typical result of the random sampling method. In this example 30 different samples were taken which were optimized separately. The blue line represents the figure of merit (FOM) for the final optimized structure of the random sampling, which is the average of the intensity at the focal point for three different wavelengths. The blue region shows the maximum and minimum intensity for all wavelengths. It is clear that there is a wide distribution in the outcome of the different samples, with a difference between the best and the worst sample of more than 15 %. To ensure that the obtained structure is close to the global optimum, the random sampling method was implemented for all 2D focusing lenses. It was not possible for the 3D structures, as those simulations are already very computational expensive.

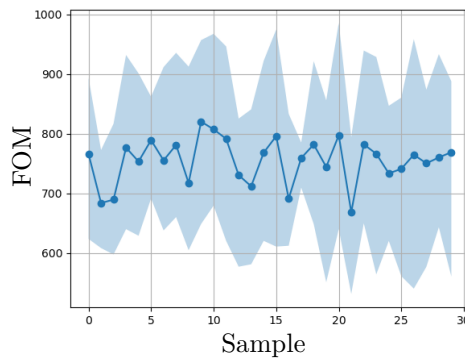


Figure 2.3: An example of the figure of merit for 30 different samples.

The second approach is to include randomization during the optimization algorithm, hereafter referred to as stochastic optimization. If the randomization is closer to the end of the optimization, it is expected that more samples are created close to the global optimum and better results can be achieved. However, as a random step from a locally optimized structure is unlikely to increase the FOM, another local optimization needs to be done after the random step. Hopefully, this brings the structure in a new local optimum. From all the random steps, the new local optima can be compared and the structure can be further optimized from the best local optimum. This algorithm is visualized in Figure 2.4.

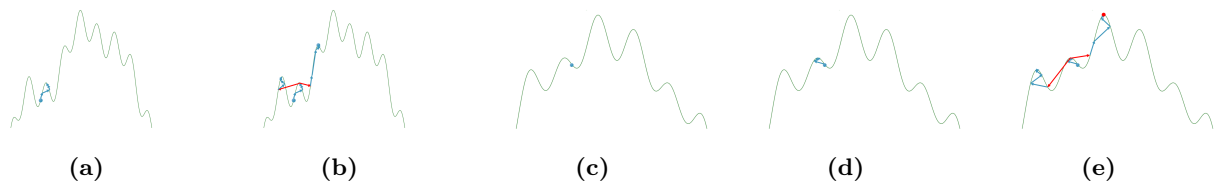


Figure 2.4: Random sampling optimization: (a) the starting structure is optimized locally, (b) from this optimum, some (2) random steps are taken (red arrows) and these new structures are again optimized locally. The best of all structures is chosen (c) the β value (see section 1.4.1) of the structure is increased, which changes the energy landscape, (d) again a local optimization is executed and (e) random steps are taken (red arrows) and these new structures are again optimized locally. The best of all structures is chosen. If the β has reached the final value, this structure is also the optimal design, if not, the steps are repeated from c.

Figure 2.5 shows an example of how the FOM evolves during the stochastic optimization. The first local optimizations with a new β are marked in red. In this example four additional random steps were taken, where after a local optimization is done before the best local optimum was selected and the β is increased. It is clear that in the start the random steps have the potential to improve the structure, however for the last three β 's, the local optima of the random steps are always worse than the initial local optimum. The random step brought the structure too far from a local optimum and no good structures could be reached within the step limit of the local optimization. As a consequence, the advantage of the stochastic optimization was not worth the additional computational expense and was thereby discarded.

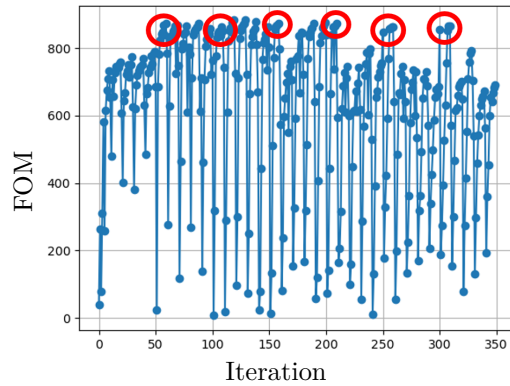


Figure 2.5: An example of the figure of merit in function of the iteration step for a stochastic optimization algorithm. The red circles mark the initial optimization after the β is increased, before a random step is taken.

2.3 Results for a 2D metalens

The study of the 2D metalens is more extensive than the study of the 3D metalens, as the optimization of the 3D structure is more computationally expensive and can take a week for one structure on twelve cores on the Imec servers. This section discusses the results of the 2D metalens and mainly the effect of the amount of layers, the minimum feature size (MFS) and the focal length.

Figure 2.6a plots the relative intensity at the focal point in function of the minimum feature size for a structure with one layer and a structure with five layers of uniform thicknesses. There is a very strong decrease in intensity with increasing MFS. The reason for this drop becomes clear with Figure 2.6b. For very large MFS (≥ 500 nm), the features of the direct design cannot be formed, so the structure performs worse than the direct design. However, for small MFS (≤ 300 nm), all features from the direct design can be formed. Additionally, while the direct design can only reach the feasible phases, the inverse design produces small gratings, much smaller than the wavelength of the light to produce an effective refractive index in between the refractive index of SiO₂

and TiO_2 and hence makes use of phase shifts that are not in the feasible phases. This is the main strength of inverse design and is much more difficult to design directly.

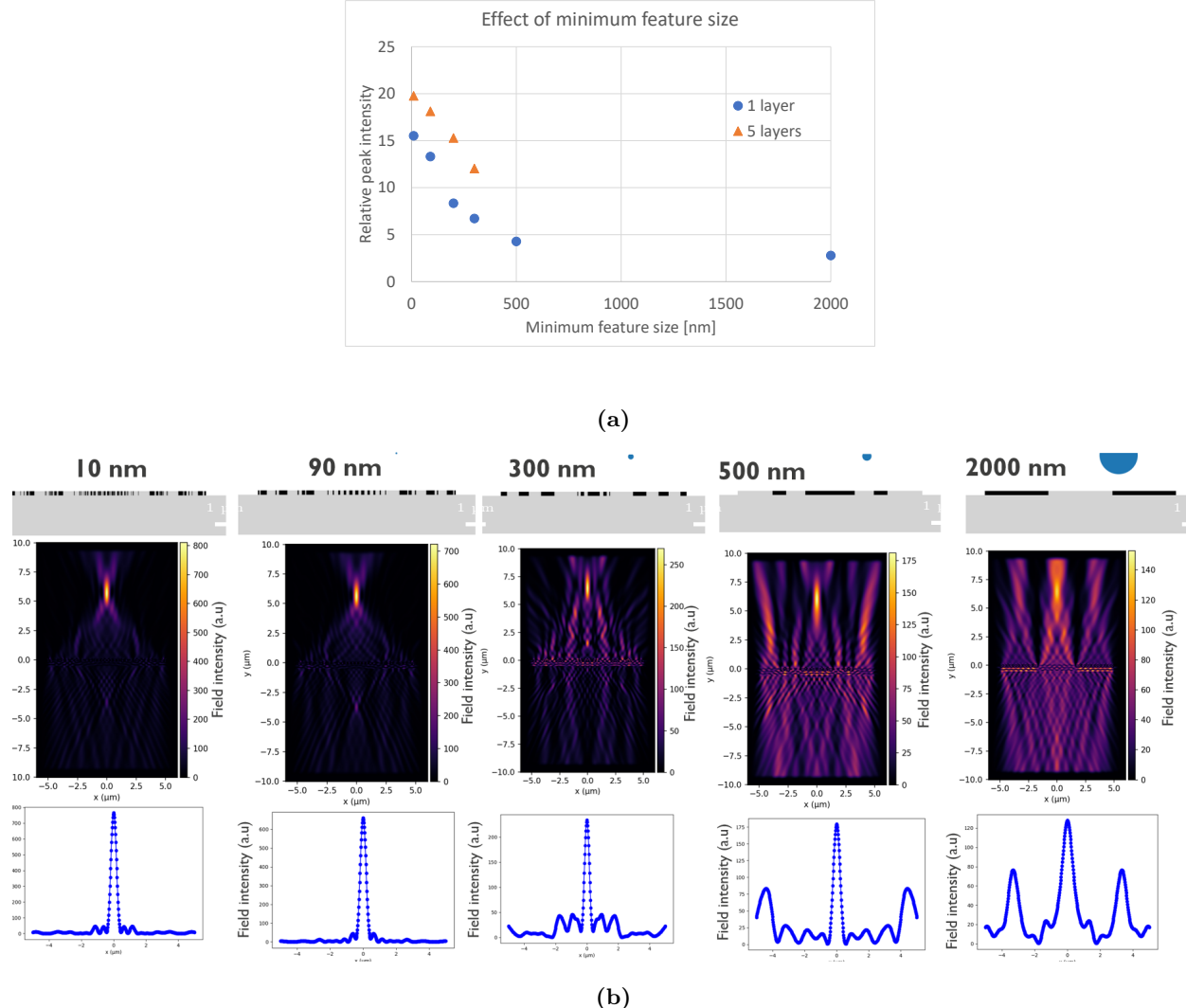


Figure 2.6: (a) Relative intensity at the focal point for the best design achieved in function of the minimum feature size for one layer and five layers (uniform thicknesses). Width $w = 10 \mu\text{m}$, focal distance $f = 6 \mu\text{m}$, average of wavelengths $\lambda = 550 \text{ nm}, 600 \text{ nm}$ and 650 nm . (b) The resulting structure, intensity in the XY-plane and intensity on the focal line for a selection of the minimum feature sizes for one layer and light with a wavelength of 600 nm . The blue circle is plotted to represent the minimum feature size.

Figure 2.7a shows the effect of the number of layers for both uniform and exponential thicknesses, for a MFS of 90 nm. The structures of the optimal designs are shown in Figure 2.8. The inverse designed structures perform better than the direct designed structures. It can be seen that for more layers, the relative intensity comes closer to the theoretical maximum of 20.99. In fact, the relative intensity for six layers is 20.69 and is thus 98.6 % "efficient" in reaching a high intensity at the focal point. Surprisingly, the exponential thicknesses only works better for two and three layers, while for four layers the exponential thicknesses performs worse than the uniform thicknesses. A possible explanation is that for a large number of layers, the features required for an optimal four layer lens with exponential thicknesses are too small. For four layers, there are $2^4 = 16$ feasible phase vectors. From Figure 1.11a it can be seen that a period of the phase spans a bit more than 1 μm on the edge of the lens. If 16 different phases on a range of 1 μm need to be achieved, the structure needs to change every 62.5 nm, which is smaller than the MFS and will therefore not be possible. As a result, for four layers or

more, having exponential thicknesses makes no sense if the MFS is equal to 90 nm.

The results for a minimum feature size of 10 nm are given in Figure 2.7b. The structures are visualised in Figure 2.9. All results are clearly better than the results obtained with a MFS of 90 nm for the same number of layers. For four layers with exponential thicknesses, the relative intensity at the focal point reaches a value of $I_f = 20.81$, which comes very close to the optimal value of 20.99. It immediately strikes the eye that the performance of structures with uniform thicknesses and exponential thicknesses is very similar. It was already concluded that for small minimum feature sizes the small features can create an intermediate refractive index and thus phases can be achieved that are not part of the theoretical feasible phases. As a result, the theory that supports exponential thicknesses to have as many feasible phases as possible is not valid anymore.

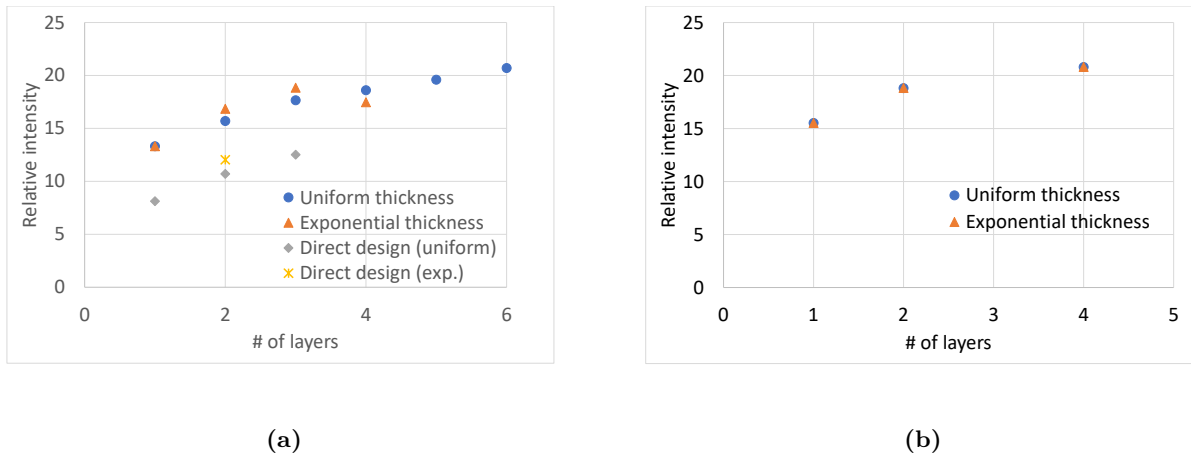


Figure 2.7: Relative intensity at the focal point for the best design achieved for a different number of layers. Width $w = 10 \mu\text{m}$, focal length $f = 6 \mu\text{m}$, average of wavelengths $\lambda = 550 \text{ nm}, 600 \text{ nm}$ and 650 nm . (a) Minimum feature size of 90 nm and (b) minimum feature of 10 nm.

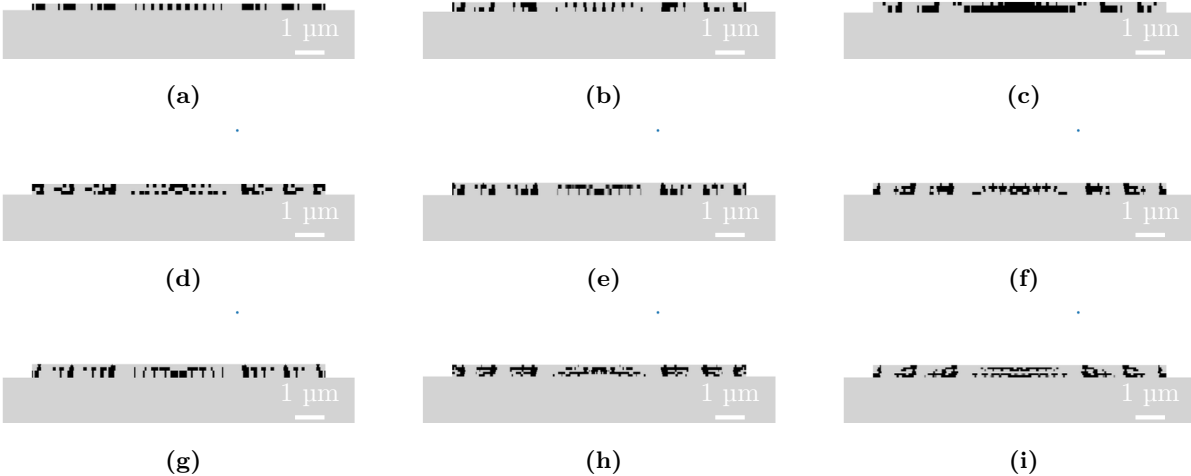


Figure 2.8: Optimal structure of the metalens with width $w = 10 \mu\text{m}$, $f = 6 \mu\text{m}$ for wavelengths $\lambda = 550, 600, 650 \text{ nm}$. (a) 1 layer, (b) 2 layers with uniform thicknesses, (c) 2 layers with exponential thicknesses, (d) 3 layers with uniform thicknesses, (e) 3 layers with exponential thicknesses, (f) 4 layers with uniform thicknesses, (g) 4 layers with exponential thicknesses, (h) 5 layers with uniform thicknesses, (i) 6 layers with uniform thicknesses.

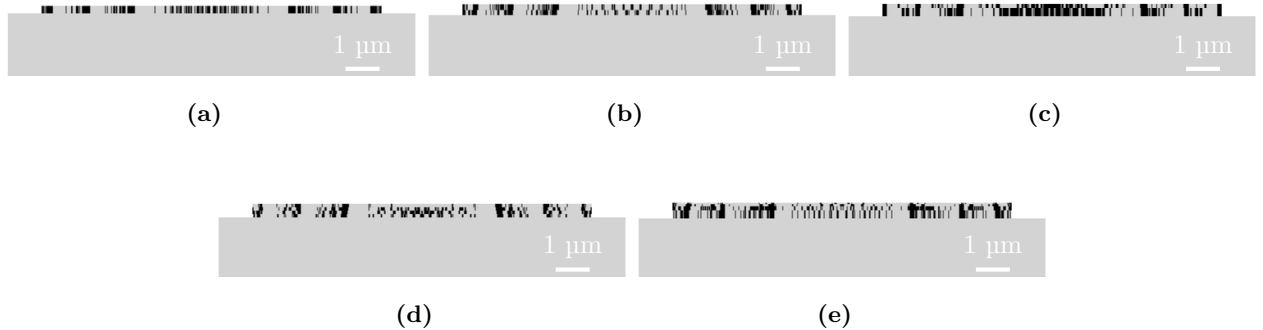


Figure 2.9: Optimal structure of the metasurface with width $w = 10 \mu\text{m}$, $f = 6 \mu\text{m}$ and a minimum feature size of 10nm for wavelengths $\lambda = 550, 600, 650 \text{ nm}$. (a) 1 layer, (b) 2 layers with uniform thicknesses, (c) 2 layers with exponential thicknesses, (d) 4 layers with uniform thicknesses and (e) 4 layers with exponential thicknesses.

Figure 2.10a shows the effect of the focal length on the relative intensity at the focal point. The experimental values were obtained by inverse design with a four layer structure with uniform thicknesses, width $w = 10 \mu\text{m}$ and a MFS of 10 nm. The reported intensity is the average of the intensity of wavelengths 550 nm, 600 nm and 650 nm. It is clear that for small focal lengths, the experimental values do not obey the theoretical model derived in section 1.2. The reason to this disparity can be derived from Figures 2.10b and 2.10c. Figure 2.10b shows the real part of the electric field. It can be seen that the field at the outer parts of the lens are transported to the center of the lens before they are deflected to the focal point. This is confirmed by Figure 2.10c, where it can be seen that the intensity inside the lens is indeed relatively large. As a result, the lens cannot be modelled as an infinitely thin device that performs a linear transformation that keeps the modules of the field constant. Instead the metasurface functions partly as a wave guide that collects the light from the source, transports the light from the outer part to the inner part to bring the light closer to the focal point and then radiates it outside the lens in the direction of the focal point. This is another example of how the inverse design achieves better results and is more versatile than direct design. The optimal design of the metasurface is shown in Figure 2.11.

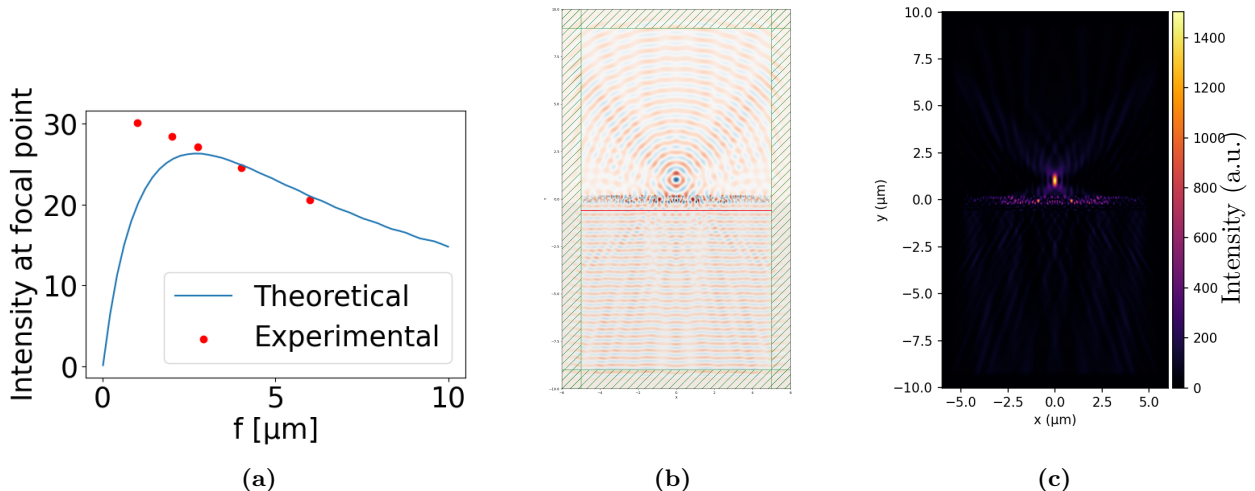


Figure 2.10: (a) The intensity at the focal point in function of the focal length (f). The line represents the theoretical value, as derived in section 1.2, while the red dots represent the values obtained with inverse design. (b) The real part of the electric field and (c) the intensity map (with arbitrary unit) for a focal length of $1 \mu\text{m}$.



Figure 2.11: Optimal design of a lens of width $w = 10 \mu\text{m}$, MFS of 10 nm, focal length $f = 1 \mu\text{m}$ and light of wavelengths 550 nm, 600 nm and 650 nm.

In this section it was shown that for a reasonable MFS of 90 nm, the structures with exponential thicknesses indeed have a better performance than the structures with uniform thicknesses. Additionally, none of the results broke the limit of a relative intensity $I_f = 20.99$ at the focal point, while some results come very close to the limit. This reinforces the theory discussed in sections 1.2 and 1.3. Only for very small minimum feature size does the theory break down as the small features can create effective intermediate refractive indices and many more phases can be created. Additionally, the strength and versatility of inverse design was illustrated in extreme conditions, like small features that can create an effective refractive index in between that of SiO_2 and TiO_2 and very small focal lengths, where the theory presented in section 1.2 breaks down and the metasurface acts partly as a waveguide to transport light.

2.4 Results for a 3D metalens

Figure 2.12 shows the results obtained by the optimization in three dimensions. The designs are given in Figure 2.13. Due to the much longer simulation times, less experiments are done. First of all, the y-axis shows that much higher relative intensities are obtained with 3D lenses compared to 2D lenses. This was expected, as the theoretical limit for 3D lenses is 390, compared to 21 for the 2D lenses. Nevertheless, the highest intensity of all lenses is 121, which is still far from the theoretical limit. Moreover, the highest intensity is acquired with direct design and not with inverse design. Additionally, all designs with two layers perform worse than the designs with only one layer. In conclusion, the 3D results are suboptimal. There are two reasons that contribute to this: first of all the 3D structures have much more degrees of freedom, which means it is more difficult to converge to the optimal structure and secondly, only one starting condition is used due to time limits, while for the 2D inverse design, the random sampling method is used, as explained in section 2.2. Overall inverse design was shown to be a very effective method to design 2D lenses. However, for 3D further work is needed to make sure the algorithm outperforms direct design. It is a possibility to explore different optimization algorithms, as was done for 2D lenses.



Figure 2.12: Relative intensity at the focal point depending on the number of layers and the type of design. Width $w = 10 \mu\text{m}$, focal length $f = 6 \mu\text{m}$, wavelength $\lambda = 600 \text{ nm}$.

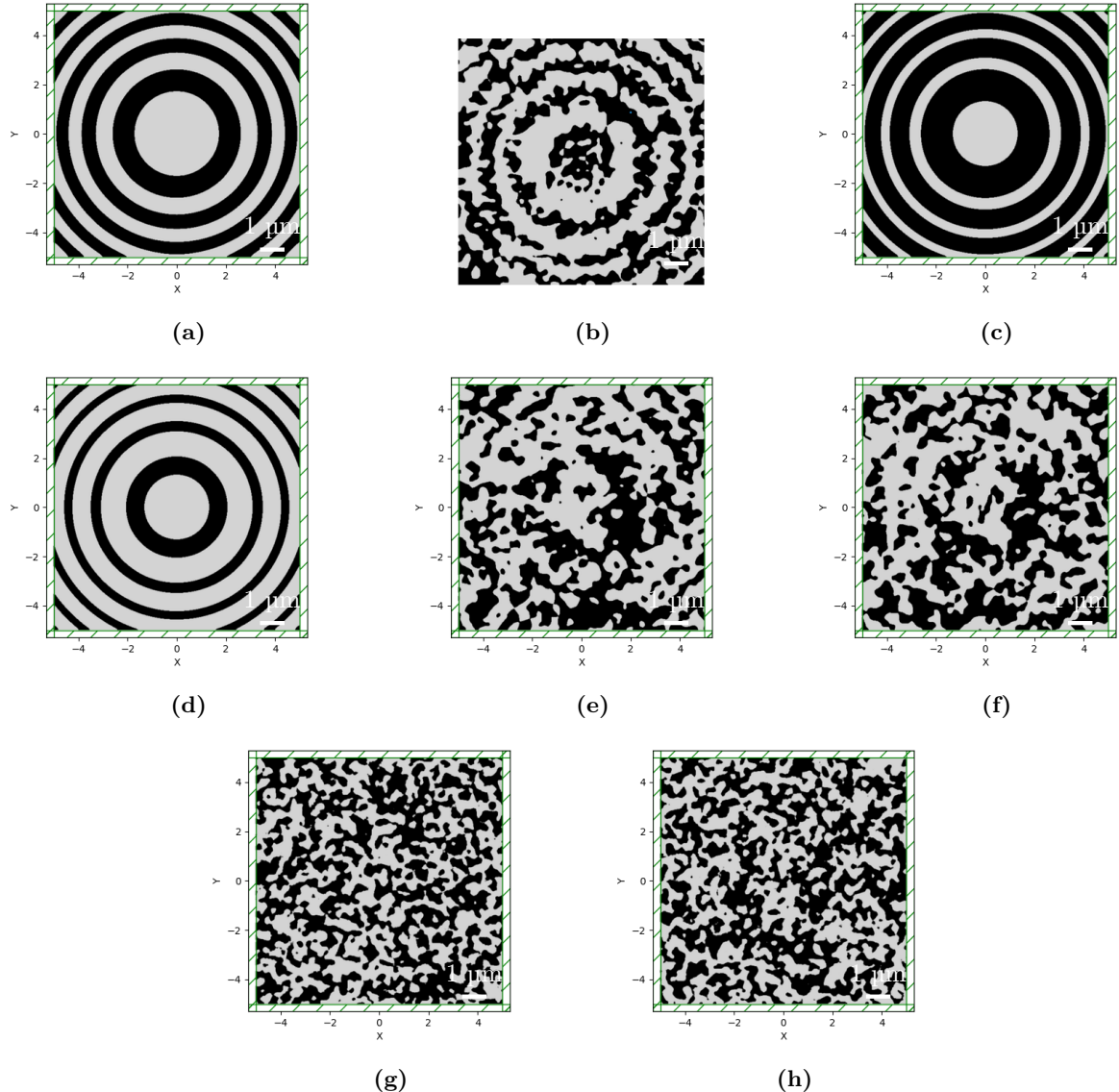


Figure 2.13: Optimal designs of a lens with width $w = 10 \mu\text{m}$, MFS of 90 nm, focal length $f = 6 \mu\text{m}$ for wavelength $\lambda = 600 \text{ nm}$. (a) 1 layer, direct design, (b) 1 layer, inverse design, (c and d) 2 uniform layers, direct design, bottom and top layer respectively. (e and f) 2 uniform layers, inverse design, bottom and top layer respectively. (g and h) 2 exponential layers, inverse design, bottom and top layer respectively.

3 Frequency splitter

The considerable amount of degrees of freedom in optical metasurfaces can be leveraged to solve new problems by exploiting their properties. This section describes the development of a frequency splitter, a metasurface that focuses different wavelengths of light at different points. Such metasurfaces could be used in imaging, where they would be included in front of the image sensor and replace the lens and filter arrays (Mansouree et al., 2020; Miyata et al., 2021).

Current digital imaging technologies use an array of photodetectors, usually based on CCDs (Charge Coupled Devices) or CMOS to capture an image and turn it into an array of electrical signals to be processed by the computer (Figure 3.1a). The incident light from the scene passes through an array of microlenses, each focusing the light onto the photodetector located underneath it. The light then passes through a color filter corresponding to either red, green or blue. With such a filter, each pixel produces an analog signal corresponding to only one of the three colors, enabling color imaging (El Gamal and Eltoukhy, 2005).

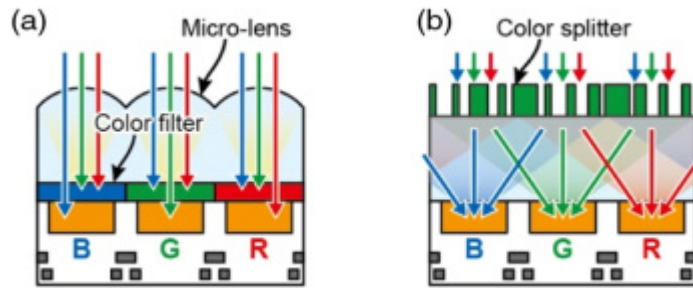


Figure 3.1: Schematic of a conventional photodetector array (a) and metalens color splitter (b) (Miyata et al., 2021).

This method suffers from optical loss, as only a fraction of the light hitting the surface of the sensor is converted to a signal for one color. The color filters are also absorptive, reducing the intensity of light even more by the time it hits the detector (Miyata et al., 2021). The use of a metalens color splitter can help solve both these issues, as depicted in Figure 3.1b. Color filters would not be needed anymore, as the incident light will already be separated by color, and the metalens allows the light hitting the entire surface to be detected.

The "dual" problem can be considered as well. Frequency splitter metasurfaces could also be applied in digital screens, where an array of LEDs emit light through an array of microlenses to project an image (Figure 3.2). Once again, losses occur at the color filters and the differently colored pixels do not cover the whole surface. By replacing the color filters with metasurfaces, one could produce pixels of any color, potentially enhancing screen resolutions, especially for near-eye displays such as in virtual reality headsets. The following table contains the

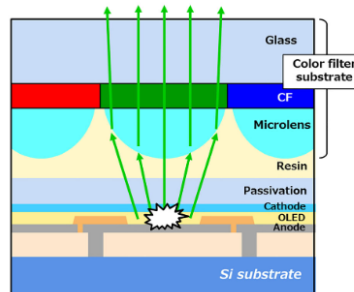


Figure 3.2: Cross-section of an OLED device with microlenses (Motoyama et al., 2019).

selected frequencies and wavelengths of light for the splitter.

Color	Frequency (10^{14} Hz)	Wavelength (nm)
Red	4.62	650
Green	5.45	550
Blue	6.38	470

Table 1: Frequencies and wavelengths of different colors.

3.1 2D splitter

The problem was first implemented in two dimensions. The resulting lenses were optimized to split two then three frequencies.

3.1.1 2 frequencies

The first attempts that were made aimed to optimize a lens consisting of only one layer, splitting two frequencies: red and blue. The resulting structure is shown in Figure 3.3, as well as the resulting electric fields.

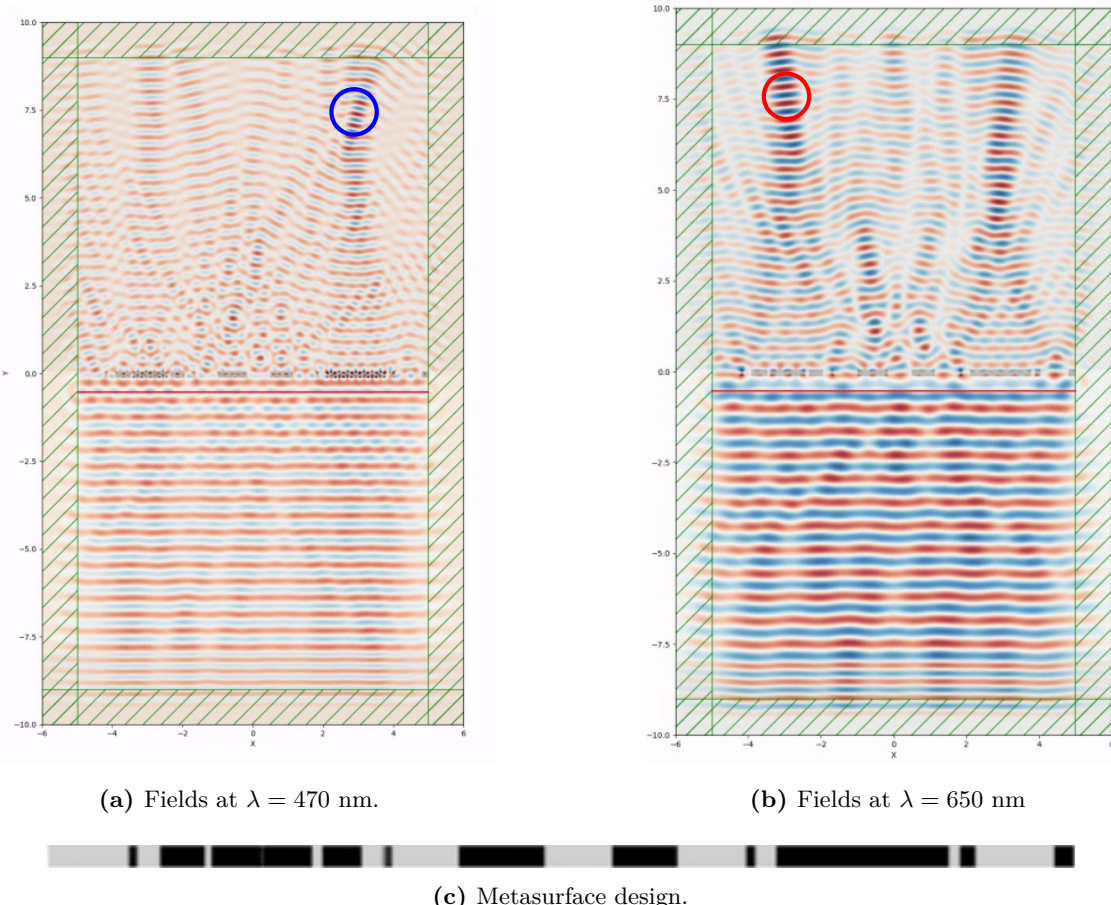


Figure 3.3: 1-layered metasurface focusing two colors. Thickness = 0.25 μm , focal point = 7 μm .

Focal points can be observed for both frequencies, but the structure struggles to keep each one focused on only one point. It was quickly realized that a multi-layered structure would reach better results, as well as enable the focusing of more frequencies by increasing the amount of degrees of freedom. The next attempts were made with up to 6 layers. The thicknesses of the layers are determined by the method described in section 1.3.3.

3.1.2 3 frequencies

To capture the entire spectrum of visible light, inspired by image sensors, the lenses were further optimized to focus green light as well. Here, the focal points are placed in a straight line, 4 μm away from the lens.

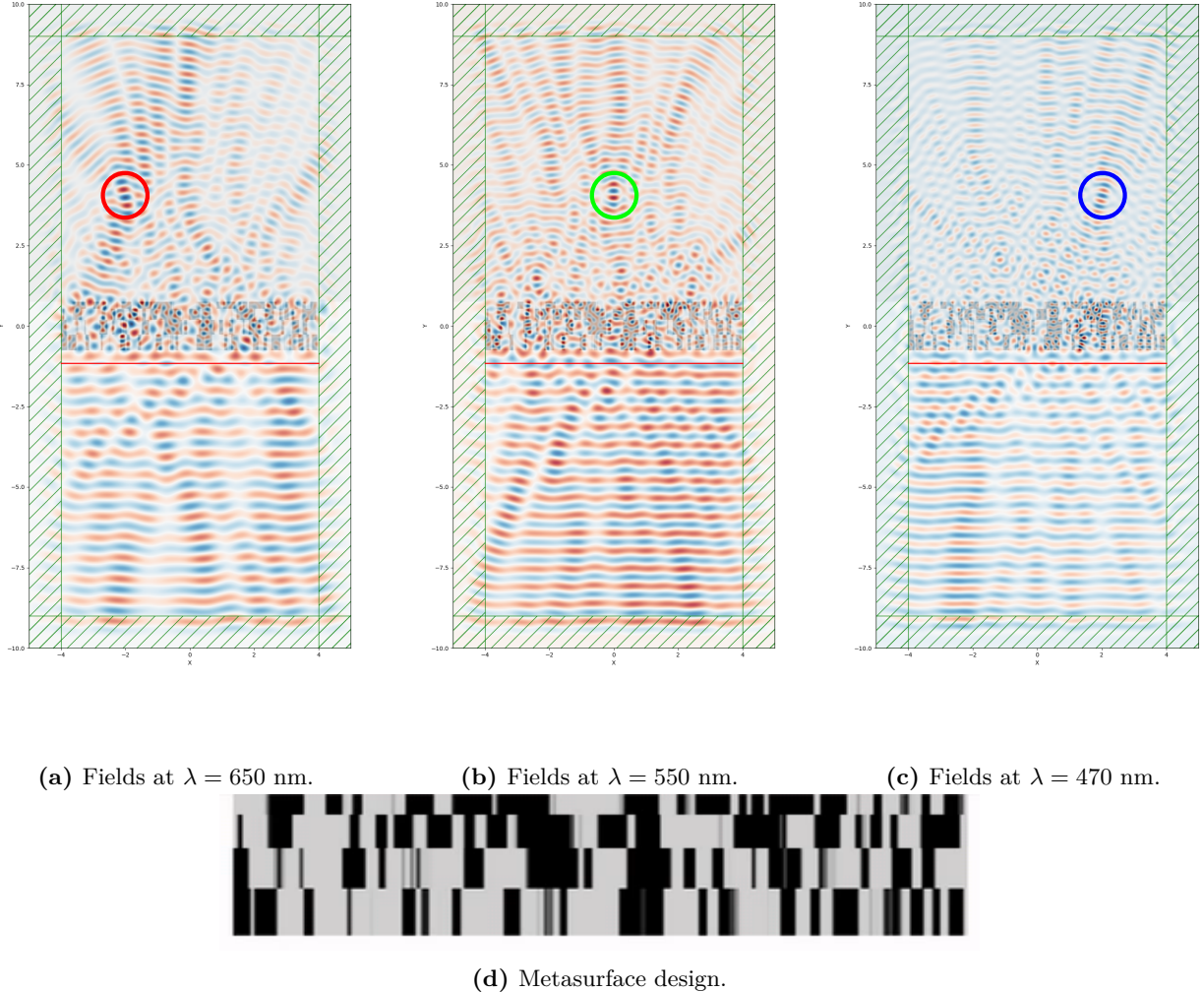


Figure 3.4: 4-layered metasurface focusing three colors. Thicknesses = 0.5, 0.445, 0.35 and 0.216 μm , focal point = 4 μm .

3.2 3D splitter

In order to design a manufacturable lens, the problem was extended to three dimensions. In this case, the focal point of the different colors were not focused in a line but were adapted to the Bayer pattern, which is used widely in conventional image sensors (Figure 3.5). In this case, the blue, red and green pixels are arranged in periodical cells of four pixels. The number of green pixels is twice that of red or blue pixels in order to mimic the human eye, which is most sensitive to green light (Bayer, 1975).

The computational cell was divided according to the purple lines in Figure 3.6 to take advantage of symmetry and reduce computational time by effectively simulating only a fourth of the total cell. The symmetry axis parallel to the y-axis was modified to reflect the electric field with a phase of 180 degrees, to preserve the E_x polarization of the source.

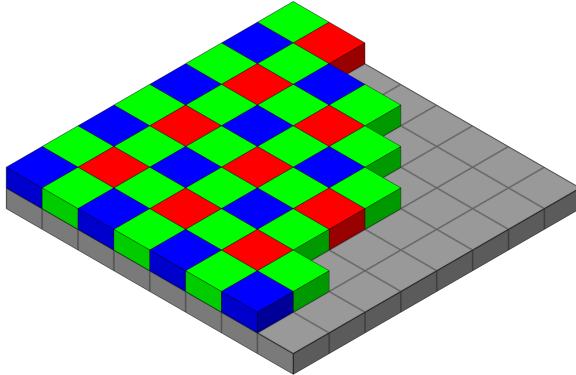


Figure 3.5: Bayer pattern for a pixel array.

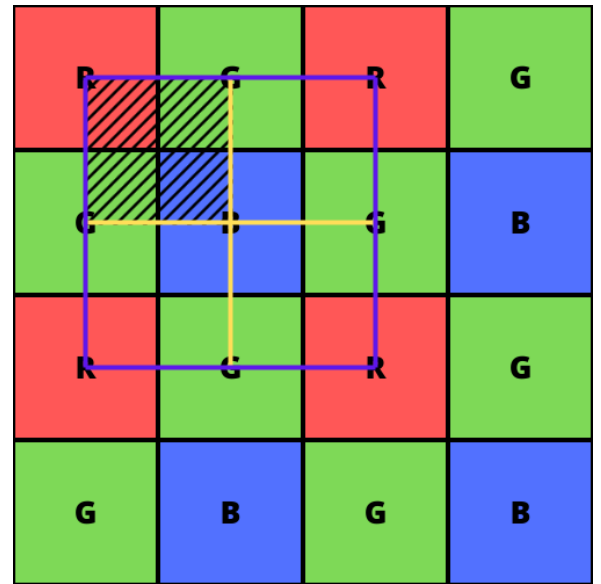


Figure 3.6: Schematic of the Bayer pattern with computational cell. The boundaries of the computational cell are represented in purple and the symmetry lines in yellow. The hatched area is the effective computational cell, after symmetrization.

The problem was first optimized for two frequencies, blue and red, at opposite corners of the computational cell. The resulting metasurface achieved an intensity of more than 12 relative to the source for the two colors (Figure 3.7). A 3-frequency splitter was then designed according to the Bayer pattern, which also included green. This time, the intensity at the focal plane was around 3.5 for all colors 3.8. To increase performance, additional layers could be added, or the lens could be made wider and thicker.

To characterize the lens, the focusing power was calculated for each part of the lens, at many different frequencies. The value of the focusing power was calculated as such:

$$\frac{\iint_C |E_{x,f}|^2 dS}{\iint_A |E_{x,s}| dS} \quad (43)$$

where C is the area of the selected color, E_f the value of the electric field at the focal point, A the area of the source (and of the entire lens) and E_s the value of the electric field at the source. This value was calculated across the visible spectrum for the three different colors of pixels (Figure 3.9).

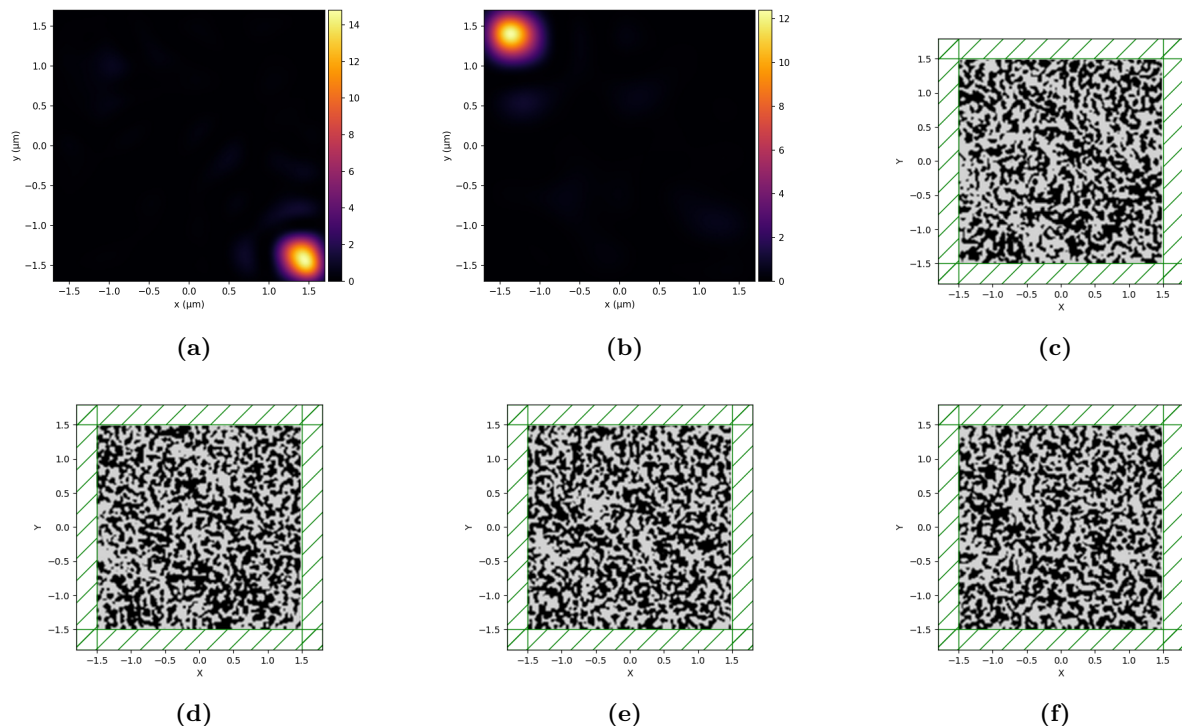


Figure 3.7: 2-frequency splitter, quarter of the total computational cell. Thicknesses = 0.487, 0.299, 0.230, 0.138 μm , focal point = 3 μm . (a, b): Relative intensity at the focal point for blue and red, respectively. (c-f): metasurface layer structure.

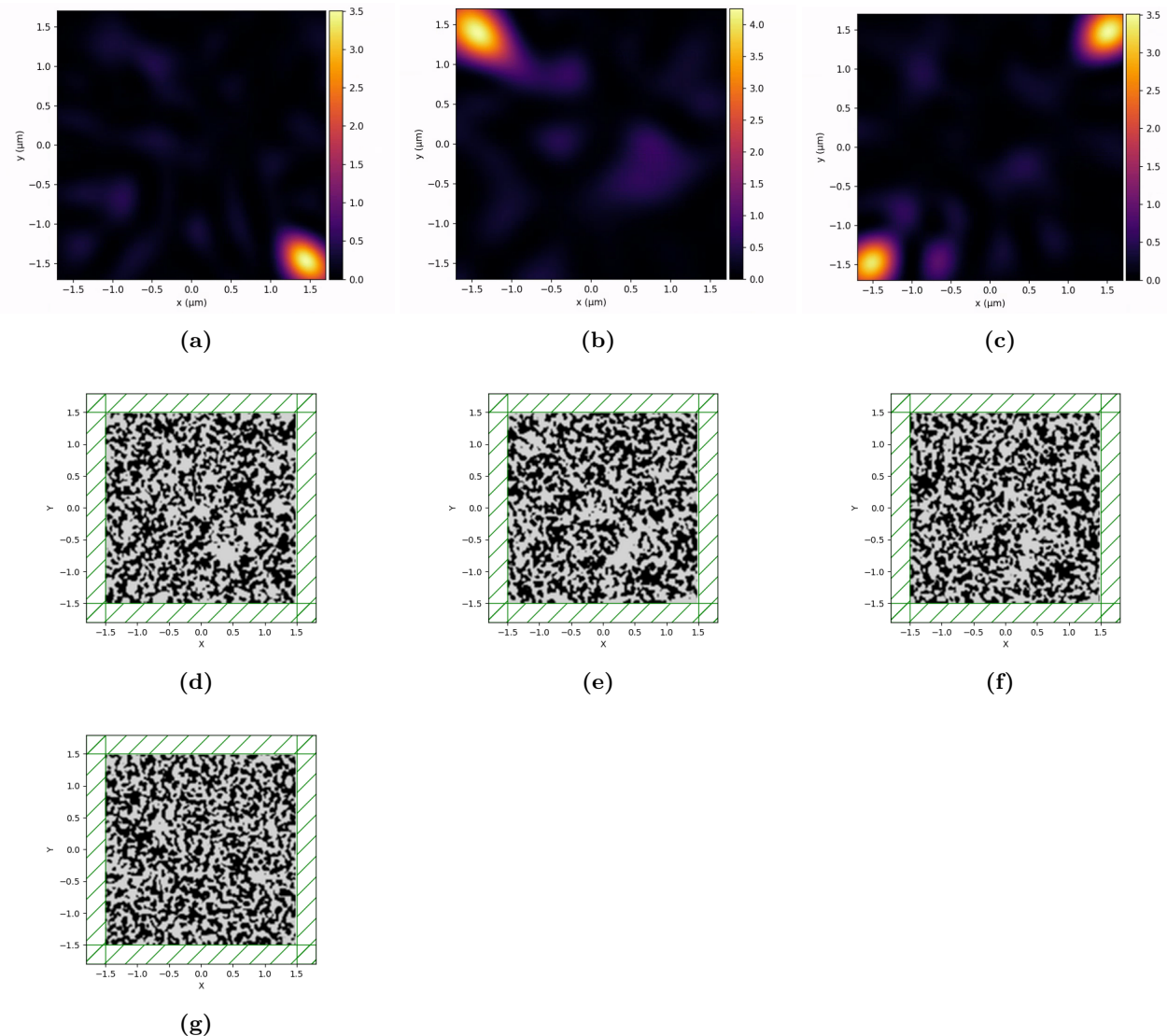


Figure 3.8: 3-frequency splitter, quarter of the total computational cell. Thicknesses = 0.4, 0.365, 0.298, 0.186 μm , focal point = 3 μm . (a-c): Relative intensity at the focal point for blue, red and green respectively. (d-g): metasurface layer structure.

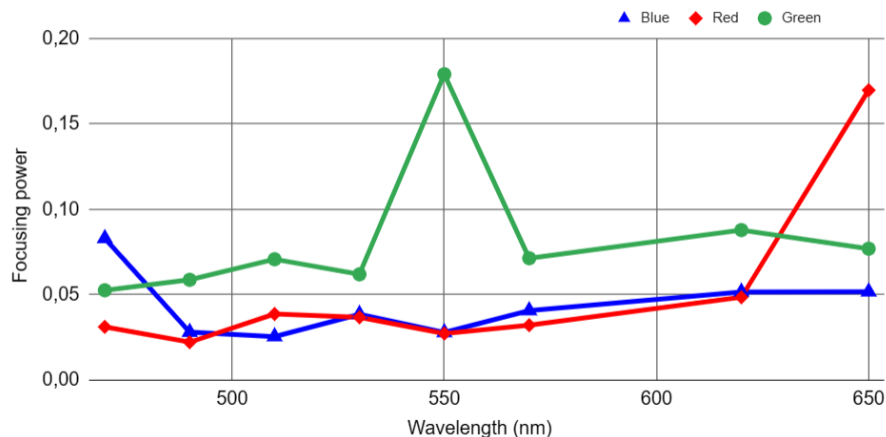


Figure 3.9: Focusing power as a function of wavelength on blue, red and green pixels.

4 Retroreflector

Retroreflectors are optical devices capable of reflecting an electromagnetic (EM) wave back along its incident direction over a continuous range of incident angles. This functionality is usually achieved by using a corner reflectors (Figure 4.1a) or Luneburg lenses. However, these conventional retroreflectors are bulky and non-planar, representing a challenge for integration and miniaturization. Therefore, planar metasurfaces would be desirable for fabrication retroreflectors for applications, such as radar cross-section augmentation, free-space communication and length measurements at microwave wavelength (Suo et al., 2022). Moreover, metasurfaces offer a range of advantages beyond their flat nature, as they enable precise control over the phase, amplitude, and polarization of EM waves at a subwavelength scale.

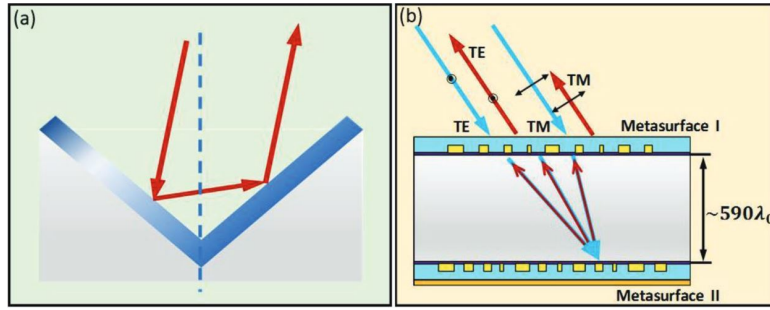


Figure 4.1: Schematic representation of: (a) bulky corner reflector. (b) cascaded metasurface (Yan et al., 2018).

To understand the operation of a retroreflector, it may be useful to compare it with other optical devices, such as a mirror and a reflective gradient metasurface. The three devices flip the direction of the normal component of the momentum of incident light. However, the mirror does not change the in-plane component of the momentum of the incident light, whereas, its sign is changed by the retroreflector and by the gradient metasurface. Besides, an in-plane momentum component is added by the latter, as shown in Figure 4.2a.

It has been reported in literature that a flat single metasurface retroreflector can produce a phase shift to the incident TE-polarized incident EM wave. But, the uniform phase gradient limits its operation to a single incident angle. Arbabi et al., 2017 described a clever set up for flat retroreflectors by using cascaded metasurfaces composed by a transmissive metasurface and a reflective metasurface (Figure 4.1b). Where the metasurface I performs a spatial Fourier transform to focus the waves with different incident angles to different spots on metasurface II. Whereas, the metasurface II acts as a gradient metasurface by adding a spatially varying momentum (Arbabi et al., 2017). This design allows the retroreflection for a continuous range of angles.

In the following subsections, the inverse design of a cascade-like retroreflector is discussed.

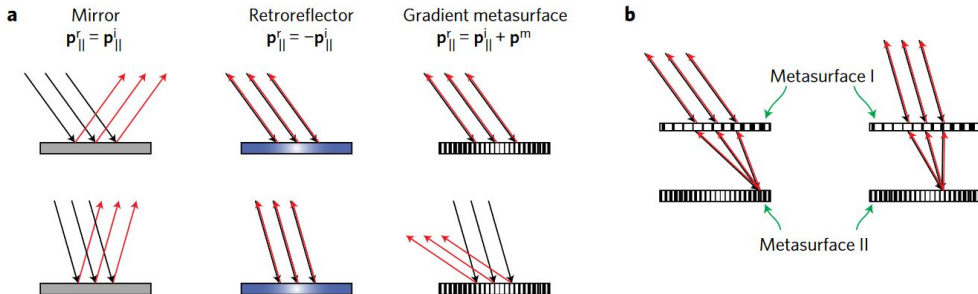


Figure 4.2: Schematic representation of: a) reflection by a mirror, a planar retroreflector and a gradient metasurface. b) planar retroreflector composed of two metasurfaces (Arbabi et al., 2017).

4.1 Problem statement

For developing an inverse design of a retroreflector, a similar optimization design to the one described by Arbabi et al., 2017 was created by using MEEP package.

The optimization design is composed of an arrangement of two metasurfaces with a slab of material in between. The materials used to design the two metasurfaces are SiO_2 and TiO_2 . While the intermediate material is SiO_2 . On the other hand, two types of boundary conditions are used: After metasurface II, metallic boundary conditions were used as a Perfect Electric Conductor (PEC) layer, representing a boundary or surface with an ideal conductivity, resulting in perfect reflection of electromagnetic waves. Meanwhile, PML was used for all the other borders.

The source used throughout the simulations is a Gaussian Source that will produce plane wavefronts at different angles and that will be located in air 0.4 micrometers away from the retroreflector. On the other hand, the monitor used to measure the fields and perform a near to far field transformation to calculate the intensity at the focal point will be located below the source. To obtain a reflected plane wavefront with the tools provided by the MEEP package, it was necessary to use a focal point at a great distance (~ 100 micrometers) from the retroreflector. This set up is shown in Figure 4.3.

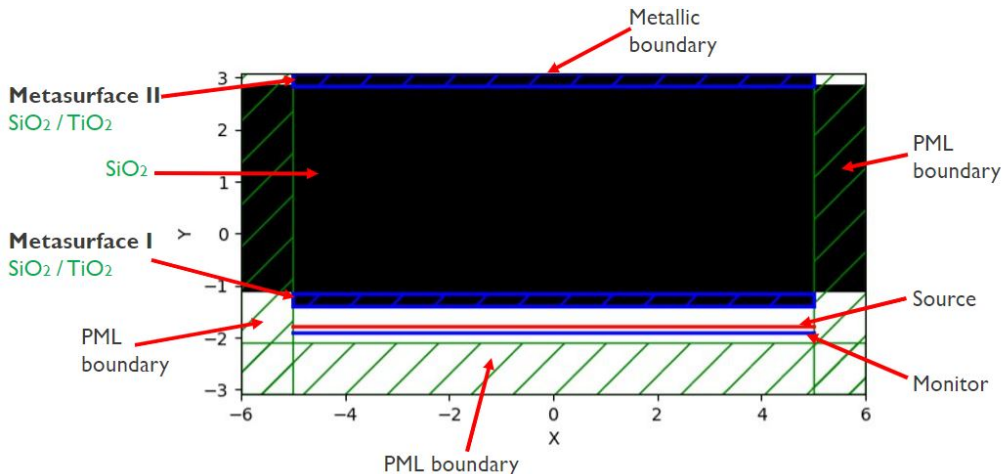


Figure 4.3: Cascaded retroreflector, optimization design.

Additionally, some parameters remained constant throughout the simulations, unless specified differently:

1. The thickness of the metasurface I is 240nm, while that of the metasurface II is 120nm, half the thickness of the first metasurface. The thickness of 240 nm was chosen to have as much control as possible over the phase as discussed in Section 1.3.2, while metasurface II is half as thick as the light passes through the surface twice.
2. The width of the metasurfaces is $10\mu\text{m}$.
3. The space between the layers (SiO_2 thickness) is $4\mu\text{m}$.
4. The wavelength used is 550 nm.
5. The minimum feature size is 90 nm.
6. Symmetry on the geometry was imposed.

For the retroreflector optimization two different approaches were used:

1. The setup shown in Figure 4.3 was used to optimize the two layers together to reflect the incident EM plane wave.

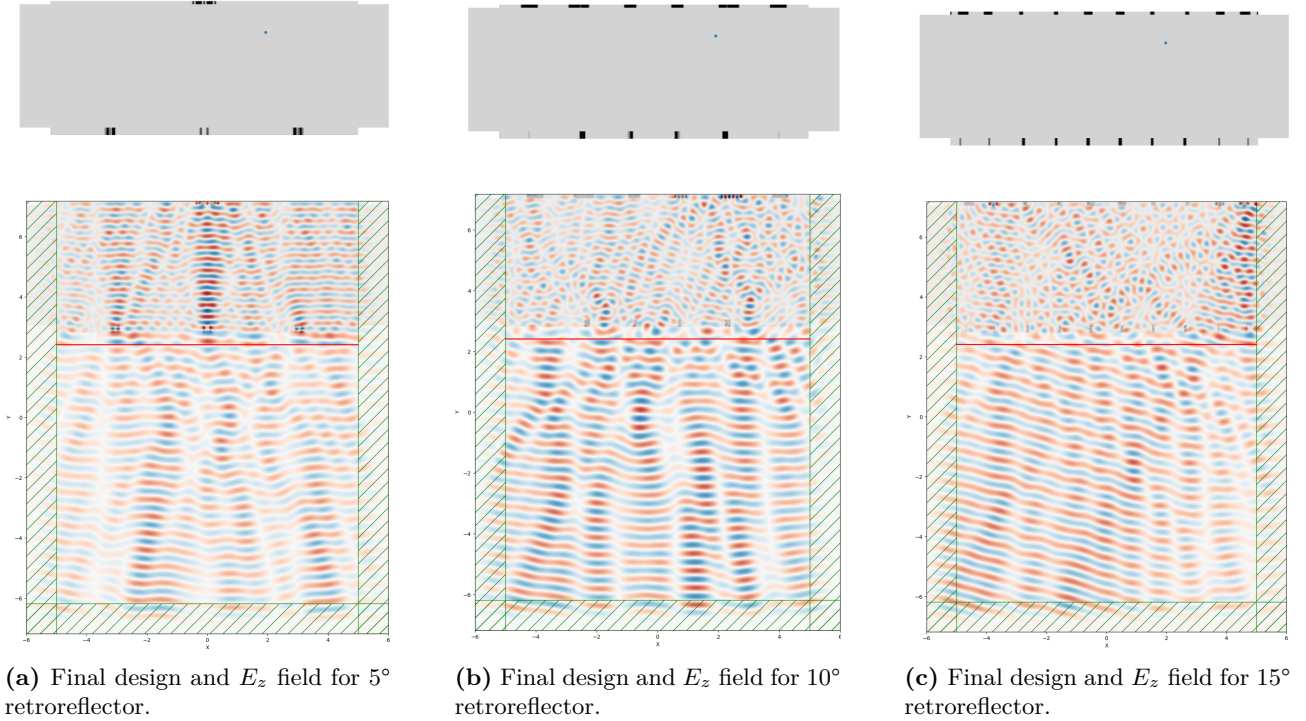


Figure 4.4: Optimized retroreflectors: Final design and E_z fields with metasurfaces I and II optimized at the same time for 5°, 10° and 15° source angle.

2. The metasurface I was first optimized to focus the incoming plane waves. This optimized metasurface was used as the input for optimizing the metasurface II to reflect the EM waves back along its incident direction. Resembling the operation principle of the cascaded retroreflector.

4.2 Results

4.2.1 First approach: Metasurfaces I and II optimized at the same time

Multiple design samples were created by varying the initial conditions of the metasurfaces, resulting in different optimized designs. These designs were evaluated based on their objective function, with the design exhibiting the highest objective function, i.e. the highest $|E_z|^2$ value, considered as the most optimal design.

Following the optimization process used by the adjoint MEEP method, the metasurfaces were successfully optimized for a wave incidence angles of 5°, 10° and 15°. Subsequently, the E_z field was plotted using this optimized design. In this section, one angle at a time was optimized, meaning that the architecture of the retroreflector will be different for each incidence angle.

Figure 4.4 shows the E_z field plots for the best design of retroreflectors with 5°, 10°, and 15° incidence angles. The retroreflector demonstrates its ability to reflect the (EM) wave back along its incident direction, from the different incidence angles. However, it is important to note that the retroreflection is not entirely flawless. The reflected wave exhibits slight deviations from perfect plane wave, and there is a gradual decrease in the intensity of the reflected electromagnetic field.

Furthermore, the solution obtained through the optimization problem using the adjoint method does not focus the incoming wave at a single point in the metasurface II. In other words, the design achieved by the solver deviates from the direct design of a retroreflector for the same configuration. This observation suggests that there is potential for enhancing the efficiency of the retroreflector by exploring new designs obtained through inverse design methodologies.

4.2.2 Second approach: Metasurfaces optimized in series

The second approach involved an incident plane EM wave with an angle of 0° for the optimization of the metasurface I and 15° for the optimization of metasurface II. In Figure 4.5a, the E_z component of the electromagnetic field is displayed for the first metasurface design, demonstrating its ability to effectively focus the field at the desired location. Figure 4.5b shows the final design of the retroreflector, revealing a focus in the metasurface II and the retroreflection of the electromagnetic field in the z direction at 15° . Nevertheless, it is evident that the reflected field is not ideal, as the front of the reflected wave exhibits significant waviness.

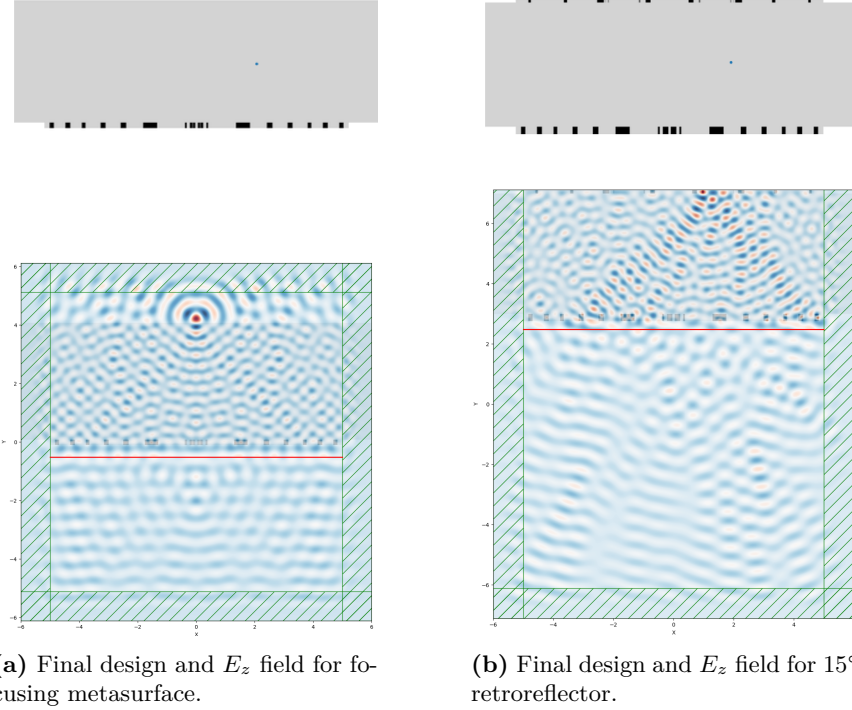


Figure 4.5: Optimized retroreflectors: Final design and E_z fields with dual metasurfaces, jointly optimized for a 15° source angle.

Upon comparing this result with the outcome obtained from the first approach, it can be concluded that the first approach yielded superior results.

4.2.3 Multiple angles

The setup of Figure 4.3 was employed to create a retroreflector with the capability to reflect incident EM waves at two distinct angles of incidence. Since MEEP does not directly support this functionality, two optimization objects were established, each associated with its respective source. During each iteration, the average of the two objective functions was calculated as the resulting objective function, while the iteration gradient was determined as the average of the gradients from both optimization objects.

The outcome is shown in Figure 4.6, revealing that the same final design of the metasurfaces is capable of retroreflecting EM waves at two different angles of incidence within specific regions, but with some imperfections persisting.

This section presents significant potential for further optimization and exploration of retroreflector designs across various applications. There are several trials that can be made to develop a better retroreflector, such as modifying the thickness of the metasurfaces, experimenting with different wavelengths, adjusting the spacing between metasurfaces, simulate a wider range of incidence angles, or even designing a retroreflector capable of retroreflecting multiple angles simultaneously. In essence, there remains a multitude of possibilities to explore and enhance the retroreflector design.

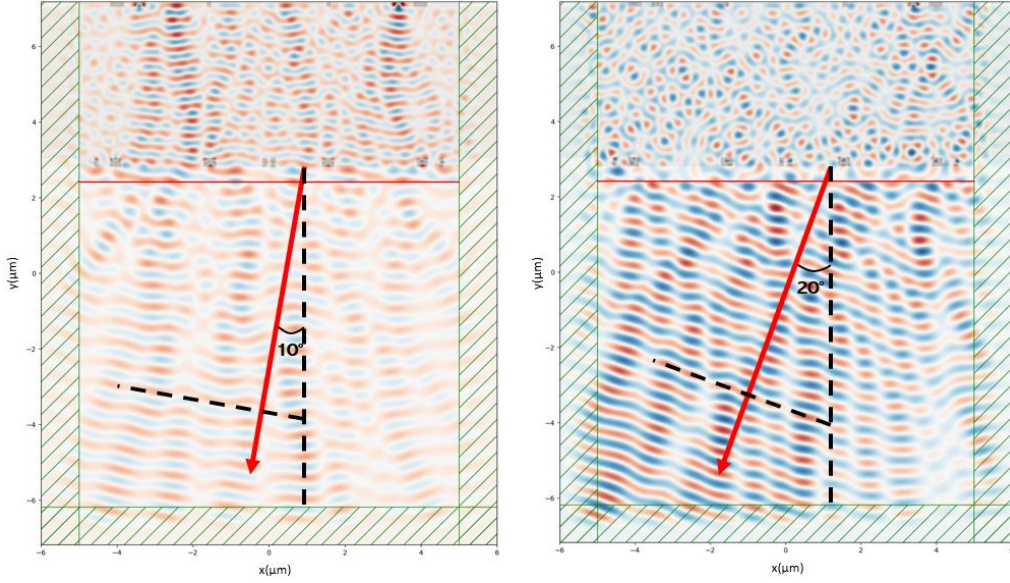
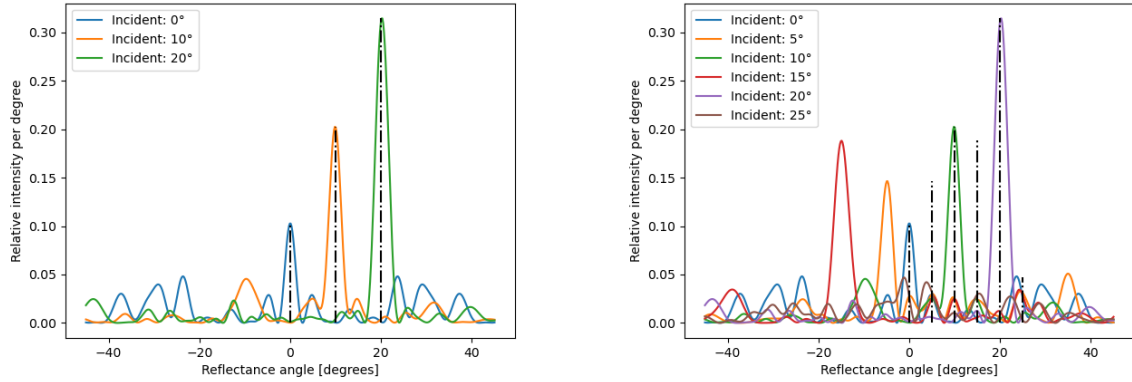


Figure 4.6: Optimized retroreflector for multiple angles: Final design and E_z fields with two metasurfaces, jointly optimized for 10° and 20° source angles.

Note: It is important to highlight that there is currently no available documentation or literature specifically addressing the inverse design of retroreflectors. Therefore, the set up and comparisons were made solely based on direct design methodologies.



(a) Relative incidence for incident wave at 0° , 10° and 20° .

(b) Relative incidence for incident wave at 0° , 5° , 10° , 15° and 20° .

Figure 4.7: Relative incidence vs angles of incidence for the retroreflector optimized for two angles

The Figures 4.7 and 4.8 show the results of the calculation of relative intensity versus reflectance angle for various incident angles. In Figure 4.7a, a noticeable peak is observed at 10° for an incidence angle of 10° , and a similar observation can be made for the 20° incidence angle. This outcome confirms the effectiveness of the optimization design of the retroreflector.

On the other hand, Figure 4.7b shows that when the optimization design for 10° and 20° is employed, and an incoming wave is directed at angles of 5° or 15° , it is reflected in a mirror-like way, by flipping the direction of the normal component of the incident light's momentum. This behavior can be attributed to the metallic boundary condition and the minimal disturbance introduced by the metasurface structures to the incoming wave. As a result, the wave is predominantly reflected by the metallic layer, leading to the observed mirror-like effect. The Figure 4.8 shows the zoomed-in intensity profile for the angles 10° and 20° .

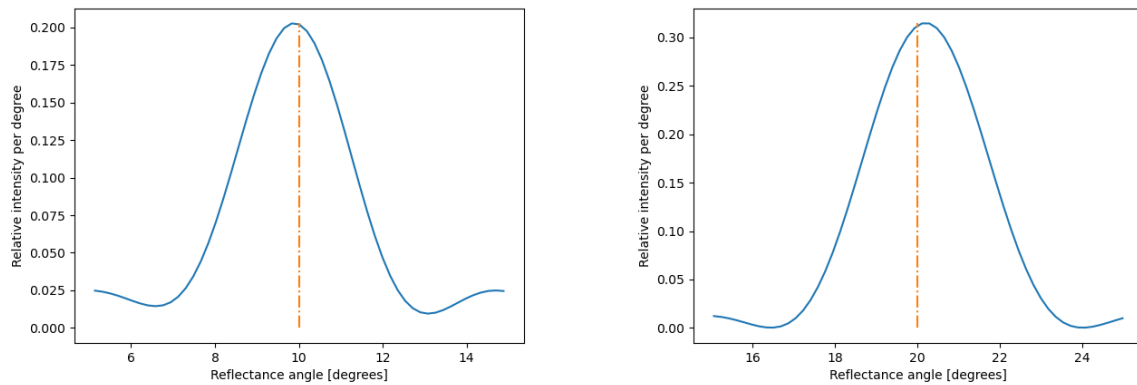


Figure 4.8: Zoomed-in intensity profile at 10° and 20° .

Finally, the calculated efficiency for 10° with an incoming wave at 10° was 0.58 and for 20° with an incoming wave at 20° was 0.93.

5 Conclusion

As photonic devices become increasingly complex, new design methodologies are needed to keep improving their functionalities. Topology optimization by the adjoint method has proven to be an effective tool to do so. This report presented three applications of optical metasurfaces, which were optimized using a design routine and compared with direct designs and their theoretical limit. Although direct design was proven to be a powerful tool to design focusing lenses and frequency splitters, inverse designed structures have a higher performance and are more versatile. Furthermore, it has been demonstrated that the adjoint method can be employed for the inverse design of retroreflectors. However, there is opportunity for further improvement of these devices by exploiting inverse design methodologies. Numerous parameters and configurations remain unexplored, presenting alternatives for continued research and refinement.

Nevertheless, there are still challenges that need to be addressed in the design of these structures, particularly in implementing the last problem in three dimensions to obtain manufacturable designs. Also for the focusing lens, better optimization algorithms need to be explored to increase the performance of the designs. A better understanding of the design constraints of standard CMOS processes is necessary to fabricate metasurfaces and test them experimentally. Furthermore, to fully exploit the potential of the adjoint method, it is important to optimize both topology and free parameters, such as layer thicknesses, using the adjoint method. By addressing these challenges, we can continue to improve the design methodologies for photonic devices and unlock their full potential.

References

- Arbabi, A., Arbabi, E., Horie, Y., Kamali, S. M., & Faraon, A. (2017). Planar metasurface retroreflector. *Nature Photonics*, 11(7), 415–420. <https://doi.org/10.1038/nphoton.2017.96>
- Arbabi, A., & Faraon, A. (2023). Advances in optical metalenses. *Nature Photonics*, 17(1), 16–25.
- Bayer, B. (1975). *Color imaging array* (US Patent 3971065A).
- El Gamal, A., & Eltoukhy, H. (2005). Cmos image sensors. *IEEE Circuits and Devices Magazine*, 21(3), 6–20. <https://doi.org/10.1109/MCD.2005.1438751>
- Fresnel, A. (1819). The wave theory of light. *Memoirs of Huygens, Young and Fresnel*, 145–156.
- Hammond, A. M., Oskooi, A., Chen, M., Lin, Z., Johnson, S. G., & Ralph, S. E. (2022). High-performance hybrid time/frequency-domain topology optimization for large-scale photonics inverse design. *Optics Express*, 30(3), 4467–4491.
- Huygens, C. (1912). *Treatise on light: In which are explained the causes of that which occurs in reflexion, & in refraction. and particularly in the strange refraction of iceland crystal*. MacMillan; Company, limited.
- Johnson, S. G. (2014). *The nlopt nonlinear-optimization package*. <http://github.com/stevengj/nlopt>
- Konijnenberg, A., Adam, A., & Urbach, P. (2021). *Bsc optics*. TU Delft Open.
- Lalau-Keraly, C. M., Bhargava, S., Miller, O. D., & Yablonovitch, E. (2013). Adjoint shape optimization applied to electromagnetic design. *Opt. Express*, 21(18), 21693–21701. <https://doi.org/10.1364/OE.21.021693>
- Mansouree, M., Kwon, H., Arbabi, E., McClung, A., Faraon, A., & Arbabi, A. (2020). Multifunctional 2.5d metastructures enabled by adjoint optimization. *Optica*, 7(1), 77–84. <https://doi.org/10.1364/OPTICA.374787>
- MEEP Documentation. (n.d.). Retrieved May 17, 2023, from <https://mEEP.readthedocs.io/en/latest/>
- Mehrabkhani, S., & Schneider, T. (2017). Is the rayleigh-sommerfeld diffraction always an exact reference for high speed diffraction algorithms? *Optics express*, 25(24), 30229–30240.
- Miller, O. (2012). *Photonic design: From fundamental solar cell, physics to computational inverse design* (Doctoral dissertation). University of California at Berkeley.
- Miyata, M., Nemoto, N., Shikama, K., Kobayashi, F., & Hashimoto, T. (2021). Full-color-sorting metalenses for high-sensitivity image sensors. *Optica*, 8(12), 1596–1604. <https://doi.org/10.1364/OPTICA.444255>
- Molesky, S., Lin, Z., Piggott, A., Jin, W., Vuckovic, J., & Rodriguez, A. (2018). Inverse design in nanophotonics. *Nature Photonics*, (12), 659–670. <https://doi.org/10.1038/s41566-018-0246-9>
- Molesky, S., Lin, Z., Piggott, A. Y., Jin, W., Vucković, J., & Rodriguez, A. W. (2018). Inverse design in nanophotonics. *Nature Photonics*, 12(11), 659–670.
- Motoyama, Y., Sugiyama, K., Tanaka, H., Tsuchioka, H., Matsusaki, K., & Fukumoto, H. (2019). High-efficiency oled microdisplay with microlens array. *Journal of the Society for Information Display*, 27(6), 354–360. <https://doi.org/https://doi.org/10.1002/jsid.784>
- Narayan, S., Divya, K. M., & Kanth, V. K. (2017). *FDTD Modeling of EM Field inside Microwave Cavities*. Springer. <https://doi.org/10.1007/978-981-10-3415-2>
- Oskooi, A. F., Roundy, D., Ibanescu, M., Bermel, P., Joannopoulos, J. D., & Johnson, S. G. (2010). Meep: A flexible free-software package for electromagnetic simulations by the fdtd method. *Computer Physics Communications*, 181(3), 687–702.
- Polyanskiy, M. N. (n.d.). *Refractive index database*. Retrieved May 13, 2023, from <https://refractiveindex.info>
- Sigmund, O., & Maute, K. (2013). Topology optimization approaches. *Structural and Multidisciplinary Optimization*, (48), 1031–1055.
- Suo, H., Ding, J., Tang, X., Chin, L. K., Qian, C., Zhu, Z., Liao, Y., Fan, Z., & Yu, Y. (2022). Wide-angle and high-efficiency flat retroreflector. *Optics Express*, 30(15), 27249. <https://doi.org/10.1364/OE.461210>
- Svanberg, K. (2002). A class of globally convergent optimization methods based on conservative convex separable approximations. *SIAM journal on optimization*, 12(2), 555–573.
- Yan, L., Zhu, W., Karim, M. F., Cai, H., Gu, A. Y., Shen, Z., Chong, P. H. J., Kwong, D.-L., Qiu, C.-W., & Liu, A. Q. (2018). 0.2 λ_0 Thick Adaptive Retroreflector Made of Spin-Locked Metasurface [eprint: <https://onlinelibrary.wiley.com/doi/pdf/10.1002/adma.201802721>]. *Advanced Materials*, 30(39), 1802721. <https://doi.org/10.1002/adma.201802721>
- Yee, K. (1966). Numerical solution of initial boundary value problems involving maxwell's equations in isotropic media. *IEEE Transactions on Antennas and Propagation*, 14(3), 302–307. <https://doi.org/10.1109/TAP.1966.1138693>
- Zhu, W., & Liu, A.-Q. (2023). *Metasurfaces: Towards Tunable and Reconfigurable Meta-devices* (Vol. 1). Springer Nature. <https://doi.org/10.1007/978-981-19-6925-6>

A Fresnel approximation

In the case that $f \ll w$, the Rayleigh-Sommerfeld integral can be approximated by replacing the r in the denominator by $r = \sqrt{(x - x')^2 + (y - y')^2 + f^2} \approx z$ and neglecting the $\frac{1}{r}$ term compared to the ik (Konijnenberg et al., 2021)

$$U_2(x', y') = -\frac{1}{2\pi} \iint_S U_1(x, y) \left(ik - \frac{1}{r} \right) \frac{e^{ikr}}{r^2} dx dy \quad (44)$$

$$\approx -\frac{1}{2\pi} \iint_S U_1(x, y) ik \frac{e^{ikr}}{f} dx dy \quad (45)$$

$$= -\frac{ik}{2\pi f} \iint_S U_1(x, y) e^{ikr} dx dy \quad (46)$$

In the nominator, r can not just be replaced by f , as all x', y' dependency would be lost. A first order Taylor expansion gives:

$$r = \sqrt{(x - x')^2 + (y - y')^2 + f^2} \quad (47)$$

$$= f \sqrt{1 + \frac{(x - x')^2 + (y - y')^2}{f^2}} \quad (48)$$

$$\approx f + \frac{(x - x')^2 + (y - y')^2}{2f} \quad (49)$$

Filling equation 49 into equation 46 gives:

$$U_2(x', y') \approx -\frac{ik e^{ikf}}{2\pi f} \iint_S U_1(x, y) e^{\frac{ik}{2f}((x-x')^2+(y-y')^2)} dx dy \quad (50)$$

$$= -\frac{ik e^{ikf} e^{\frac{ik}{2f}(x'^2+y'^2)}}{2\pi f} \iint_S U_1(x, y) e^{\frac{ik}{f}(x'x+y'y)} e^{\frac{ik}{2f}(x^2+y^2)} dx dy \quad (51)$$

This integral represents a Fourier transform

$$U_2(x', y') \approx -\frac{ik e^{ikf} e^{\frac{ik}{2f}(x'^2+y'^2)}}{2\pi f} \mathcal{F} \left\{ U_1(x, y) e^{\frac{ik}{2f}(x^2+y^2)} \right\} \left(\frac{kx'}{2\pi f}, \frac{ky'}{2\pi f} \right) \quad (52)$$

This is the Fresnel approximation. The Fraunhofer approximation goes a bit further by dropping the Fresnel propagator $e^{\frac{ik}{2f}(x^2+y^2)}$ in the Fourier transform for $x^2 + y^2 \ll 2f/k$. (Konijnenberg et al., 2021)

$$U_2(x', y') \approx -\frac{ik e^{ikf} e^{\frac{ik}{2f}(x'^2+y'^2)}}{2\pi f} \mathcal{F} \{ U_1(x, y) \} \left(\frac{kx'}{2\pi f}, \frac{ky'}{2\pi f} \right) \quad (53)$$

Additionally, k can be replaced by its definition $k = \frac{2\pi}{\lambda}$ and the factor $ie^{ikf} e^{\frac{ik}{2f}(x'^2+y'^2)}$ can be dropped, as we are not interested in the off-set of the phase.

$$U_2(x', y') \approx -\frac{1}{\lambda f} \mathcal{F} \{ U_1(x, y) \} \left(\frac{x'}{\lambda f}, \frac{y'}{\lambda f} \right) \quad (54)$$

Equation 54 is the most famous equation to describe the effect of lenses. However, this equation is not valid for the metasurfaces studies in this report. Namely the Fresnel approximation requires that $r \approx f$, while for typical values $f = 6 \text{ } \mu\text{m}$ and $w = 10 \text{ } \mu\text{m}$: $r \leq \sqrt{f^2 + (\frac{w}{2})^2} = 7.81 \text{ } \mu\text{m} \not\approx f = 6 \text{ } \mu\text{m}$. As a consequence, incorporating the Fresnel approximation can give rise to errors up to 30 %. The Fraunhofer approximation requires that $x^2 + y^2 \ll 2f/k = f\lambda/\pi$, while for $f = 6 \text{ } \mu\text{m}$, $w = 10 \text{ } \mu\text{m}$ and $\lambda = 0.6 \text{ } \mu\text{m}$: $x^2 + y^2 \leq (\frac{w}{2})^2 = 25 \text{ } \mu\text{m}^2 \not\ll \frac{f\lambda}{\pi} = 1.15 \text{ } \mu\text{m}^2$.

As the Fraunhofer approximation is way too coarse, it will not be discussed any further. However, the Fresnel approximation will still have a qualitative agreement with the exact solution and is worth exploring further. From equation 52, again the phase off-set $ie^{ikf} e^{\frac{ik}{\lambda f}(x'^2+y'^2)}$ can be dropped and k can be replaced by its definition $k = \frac{2\pi}{\lambda}$.

$$U_2(x', y') \approx -\frac{1}{\lambda f} \mathcal{F} \left\{ U_1(x, y) e^{\frac{i\pi}{\lambda f}(x^2+y^2)} \right\} \left(\frac{x'}{\lambda f}, \frac{y'}{\lambda f} \right) \quad (55)$$

To calculate the field in the focal plane ($U_2(x', y')$), the field behind the lens ($U_1(x, y)$) needs to be filled into equation 55. First, the optimal field behind the lens given by equation 12 can be approximated again by assuming $r' = \sqrt{x^2 + y^2 + f^2} \approx f + \frac{x^2+y^2}{2f}$.

$$U_1(x, y) = \begin{cases} e^{-i\frac{2\pi}{\lambda}r'} & |x| \text{ and } |y| \leq \frac{w}{2} \\ 0 & |x| \text{ or } |y| > \frac{w}{2} \end{cases} \quad (56)$$

$$\approx \begin{cases} e^{-i\frac{2\pi f}{\lambda}} e^{-i\frac{2\pi}{\lambda} \frac{x^2+y^2}{2f}} & |x| \text{ and } |y| \leq \frac{w}{2} \\ 0 & |x| \text{ or } |y| > \frac{w}{2} \end{cases} \quad (57)$$

$$= \begin{cases} e^{-i\frac{\pi}{\lambda f}(x^2+y^2)} & |x| \text{ and } |y| \leq \frac{w}{2} \\ 0 & |x| \text{ or } |y| > \frac{w}{2} \end{cases} \quad (58)$$

Where again the phase off-set $e^{-i\frac{2\pi f}{\lambda}}$ was dropped. Filling in equation 58 into equation 55 gives:

$$U_2(x', y') \approx -\frac{1}{\lambda f} \mathcal{F} \left[\begin{cases} e^{-i\frac{\pi}{\lambda f}(x^2+y^2)} e^{\frac{i\pi}{\lambda f}(x^2+y^2)} & |x| \text{ and } |y| \leq \frac{w}{2} \\ 0 & |x| \text{ or } |y| > \frac{w}{2} \end{cases} \right] \left(\frac{x'}{\lambda f}, \frac{y'}{\lambda f} \right) \quad (59)$$

$$= -\frac{1}{\lambda f} \mathcal{F} \left[\begin{cases} 1 & |x| \text{ and } |y| \leq \frac{w}{2} \\ 0 & |x| \text{ or } |y| > \frac{w}{2} \end{cases} \right] \left(\frac{x'}{\lambda f}, \frac{y'}{\lambda f} \right) \quad (60)$$

Similarly, for a 2D lens using the same derivation as above, it can be shown that $U_1(x') = \begin{cases} e^{-i\frac{\pi}{\lambda f}x^2} & |x| \text{ and } |y| \leq \frac{w}{2} \\ 0 & |x| \text{ or } |y| > \frac{w}{2} \end{cases}$.

$$U_2(x') \approx -\frac{1}{\sqrt{\lambda f}} \mathcal{F} \left[\begin{cases} 1 & |x| \leq \frac{w}{2} \\ 0 & |x| > \frac{w}{2} \end{cases} \right] \left(\frac{x'}{\lambda f} \right) \quad (61)$$

$$= \frac{\sqrt{\lambda f}}{\pi} \frac{\sin\left(\frac{\pi w x'}{\lambda f}\right)}{x'} \quad (62)$$

And the relative intensity at the focal line is

$$I_2(x') = U_2(x')^2 \quad (63)$$

$$= \frac{\lambda f}{\pi^2} \frac{\sin^2\left(\frac{\pi w x'}{\lambda f}\right)}{(x')^2} \quad (64)$$

$$I_2(0) = \frac{\lambda f}{\pi^2} \left(\frac{\pi w}{\lambda f} \right)^2 \quad (65)$$

$$= \frac{w^2}{\lambda f} \quad (66)$$

For $f = 6 \mu\text{m}$, $w = 10 \mu\text{m}$ and $\lambda = 0.6 \mu\text{m}$, the optimal relative intensity at the focal point is 27.8 compared to the intensity of the source.

B Analytical derivation of the intensity at the focal point

B.1 Intensity for a circular lens

At the focal point $x' = y' = 0$, and thus $r = r' = \sqrt{f^2 + u^2}$ (with $u^2 = x^2 + y^2$) and $\cos(\theta) = \frac{f}{r}$, resulting in:

$$U_2(0,0) = -\frac{1}{2\pi} \iint_S \left(ik - \frac{1}{r} \right) \frac{f}{r^2} dx dy \quad (67)$$

$$(68)$$

Conversion to polar coordinates gives

$$U_2(0,0) = -\frac{1}{2\pi} \int_0^{2\pi} d\alpha \int_0^{\frac{w}{2}} \left(ik - \frac{1}{\sqrt{u^2 + f^2}} \right) \frac{fu}{u^2 + f^2} du \quad (69)$$

$$= ik \int_0^{\frac{w}{2}} \frac{fu}{u^2 + f^2} du - \int_0^{\frac{w}{2}} \frac{fu}{(u^2 + f^2)^{3/2}} du \quad (70)$$

Using the substitution $v = u^2 + f^2$ and $dv = 2udu$ gives:

$$U_2(0,0) = \frac{ik}{2} \int_{f^2}^{\left(\frac{w}{2}\right)^2 + f^2} \frac{f}{v} dv - \frac{1}{2} \int_{f^2}^{\left(\frac{w}{2}\right)^2 + f^2} \frac{f}{(v)^{3/2}} dv \quad (71)$$

$$= \frac{ikf}{2} \ln \left[1 + \left(\frac{w}{2f} \right)^2 \right] - \frac{f}{2} \left[\frac{1}{f} - \frac{1}{\sqrt{\left(\frac{w}{2}\right)^2 + f^2}} \right] \quad (72)$$

$$= \frac{ikf}{2} \ln \left[1 + \left(\frac{w}{2f} \right)^2 \right] - \frac{1}{2} \left[1 - \frac{1}{\sqrt{1 + \left(\frac{w}{2f} \right)^2}} \right] \quad (73)$$

And the intensity at the focal point I_f is then:

$$I_f = \left\{ \frac{kf}{2} \ln \left[1 + \left(\frac{w}{2f} \right)^2 \right] \right\}^2 + \frac{1}{4} \left[1 - \frac{1}{\sqrt{1 + \left(\frac{w}{2f} \right)^2}} \right]^2 \quad (74)$$

$$= \left\{ \frac{\pi f}{\lambda} \ln \left[1 + \left(\frac{w}{2f} \right)^2 \right] \right\}^2 + \frac{1}{4} \left[1 - \frac{1}{\sqrt{1 + \left(\frac{w}{2f} \right)^2}} \right]^2 \quad (75)$$

In case $\left(\frac{\pi f}{\lambda} \right)^2 \gg 1$, the second term can be neglected. Typical values in this study are $f = 6 \mu\text{m}$ and $\lambda = 0.6 \mu\text{m}$. Which gives $\left(\frac{\pi f}{\lambda} \right)^2 \approx 10^3 \gg 1$. The intensity can thus be approximated as:

$$I_f = \left\{ \frac{\pi f}{\lambda} \ln \left[1 + \left(\frac{w}{2f} \right)^2 \right] \right\}^2 \quad (76)$$

B.2 Intensity for a rectangular lens

For a square lens, the integral can be simplified by a transformation to polar coordinates and only considering the part $\theta \in [0, \pi/4]$ and multiplying that by eight, as indicated in figure B.1.

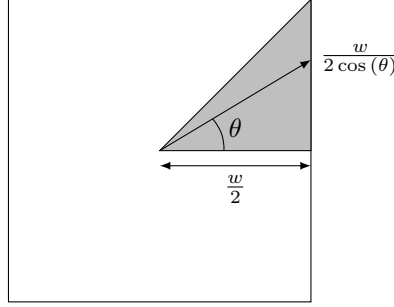


Figure B.1: Integration region for a square lens with width w .

$$U_2(0,0) = -8 \frac{ik}{2\pi} \int_0^{\frac{\pi}{4}} d\theta \int_0^{\frac{w}{2 \cos \theta}} \frac{fu}{f^2 + u^2} du \quad (77)$$

Using the substitution $v = u^2 + f^2$ with $dv = 2udu$ gives:

$$U_2(0,0) = -\frac{2ik}{\pi} \int_0^{\frac{\pi}{4}} d\theta \int_{f^2}^{f^2 + (\frac{w}{2 \cos \theta})^2} \frac{f}{v} dv \quad (78)$$

$$= -\frac{2ikf}{\pi} \int_0^{\frac{\pi}{4}} \ln \left[1 + \left(\frac{w}{2f \cos \theta} \right)^2 \right] d\theta \quad (79)$$

This expression cannot be calculated analytically, the analytical result for $f = 6 \text{ } \mu\text{m}$, $w = 10 \text{ } \mu\text{m}$ and $\lambda = 0.6 \text{ } \mu\text{m}$ is $|U_2(0,0)| = 19.75$ and thus $I_f(0,0) = 389.96$. Another possibility is to approximate the integrand by a fifth order Taylor expansion by using the derivatives of appendix D. This allows to make quick approximate calculations (with an error less than 2 %). The Taylor expansion is plotted in figure B.2 and shows the correspondens between the fourth/fifth order expansion and the exact integrand.

$$U_2(0,0) = -\frac{2ikf}{\pi} \int_0^{\frac{\pi}{4}} \left\{ \ln \left[1 + \left(\frac{w}{2f} \right)^2 \right] + \frac{\theta^2}{1 + \left(\frac{2f}{w} \right)^2} + \frac{1 + 4 \left(\frac{2f}{w} \right)^2}{6 \left[1 + \left(\frac{2f}{w} \right)^2 \right]^2} \theta^4 + O(\theta^6) \right\} d\theta \quad (80)$$

$$\approx -\frac{ikf}{2} \left\{ \ln \left[1 + \left(\frac{w}{2f} \right)^2 \right] + \frac{1}{1 + \left(\frac{2f}{w} \right)^2} \frac{\pi^2}{48} + \frac{1 + 4 \left(\frac{2f}{w} \right)^2}{\left[1 + \left(\frac{2f}{w} \right)^2 \right]^2} \frac{\pi^4}{7680} \right\} \quad (81)$$

Finally, the intensity is given by:

$$I_f(0,0) \approx \frac{k^2 f^2}{4} \left\{ \ln \left[1 + \left(\frac{w}{2f} \right)^2 \right] + \frac{1}{1 + \left(\frac{2f}{w} \right)^2} \frac{\pi^2}{48} + \frac{1 + 4 \left(\frac{2f}{w} \right)^2}{\left[1 + \left(\frac{2f}{w} \right)^2 \right]^2} \frac{\pi^4}{7680} \right\}^2 \quad (82)$$

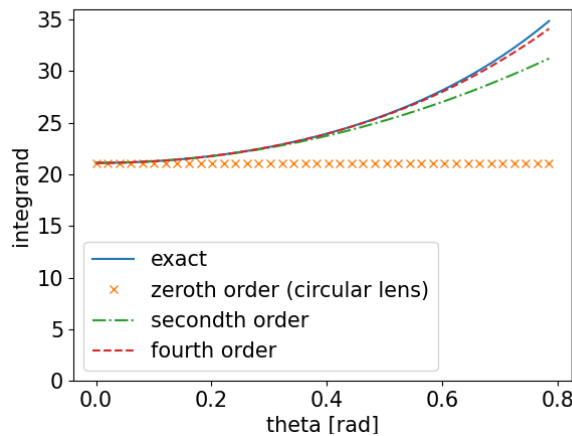


Figure B.2: Taylor series approximations for the integrand. The zeroth order Taylor expansion would give the same solution as the circular lens. The fourth/fifth order Taylor expansion is used to approximate the integral.

C Gaussian source in Meep

The Gaussian source is defined in time-domain as:

$$U_0 = \frac{1}{i\omega} \frac{\partial}{\partial t} \exp \left(-i\omega t - \frac{(t-t_0)^2}{2w^2} \right) \quad (83)$$

$$= \frac{1}{i\omega} \left(-i\omega - \frac{t-t_0}{w^2} \right) \exp \left(-i\omega t - \frac{(t-t_0)^2}{2w^2} \right) \quad (84)$$

With $w = 1/f_w$ the reciprocal of fwidth (f_w).

The fourier transform is then

$$\tilde{U}_0 = \mathcal{F} \left\{ \frac{1}{i\omega_0} (-i\omega_0 - f_w^2(t-t_0)) \exp \left(-i\omega_0 t - \frac{(t-t_0)^2}{2} f_w^2 \right) \right\} \quad (85)$$

$$= \frac{\omega}{\omega_0 f_w} \exp \left(-\frac{1}{2} \frac{(\omega - \omega_0)^2}{f_w^2} \right) \quad (86)$$

So, the peak field should be $\tilde{U}_0(\omega = \omega_0) = \frac{1}{f_w^2}$, so the intensity scales with $I \sim \frac{1}{f_w^2}$. Corresponding to experiments, $I = 0.04074/f_w^2$. However, the intensity depends highly on the material and structure. For example, $I \sim \frac{1}{n^2}$, with n the refractive index of the material where the source is located, but it is also depend on other materials in the neighbourhood of the source. Meep's documentation is not clear about the intensity of the source.

D Taylor series

$$f(\theta) = \ln \left[1 + \left(\frac{a}{\cos \theta} \right)^2 \right] \quad (87)$$

$$f(0) = \ln(1 + a^2) \quad (88)$$

$$\frac{df(\theta)}{d\theta} = \frac{a^2}{1 + \left(\frac{a}{\cos \theta} \right)^2} \frac{2 \sin(\theta)}{\cos^3(\theta)} \quad (89)$$

$$= \frac{2a^2 \sin(\theta)}{\cos^3(\theta) + a^2 \cos(\theta)} \quad (90)$$

$$\frac{df(0)}{d\theta} = 0 \quad (91)$$

$$\frac{d^2 f(\theta)}{d\theta^2} = \frac{2 \cos^2(\theta) [1 + b^2 \cos^2(\theta)] + 2 \sin^2(\theta) [1 + 3b^2 \cos^2(\theta)]}{[\cos(\theta) + b^2 \cos^3(\theta)]^2} \quad \text{with } b = \frac{1}{a} \quad (92)$$

$$= \frac{2 [1 + b^2 \cos^2(\theta)] + 4b^2 \sin^2(\theta) \cos^2(\theta)}{[\cos(\theta) + b^2 \cos^3(\theta)]^2} \quad (93)$$

$$= \frac{2 [1 + b^2 \cos^2(\theta)] + b^2 \sin^2(2\theta)}{[\cos(\theta) + b^2 \cos^3(\theta)]^2} \quad (94)$$

$$\frac{d^2 f(0)}{d\theta^2} = \frac{2(1 + b^2)}{(1 + b^2)^2} = \frac{2}{1 + b^2} \quad (95)$$

$$\frac{d^3 f(\theta)}{d\theta^3} = \frac{[\cos(\theta) + b^2 \cos^3(\theta)]^2 [-4b^2 \sin(\theta) \cos(\theta) + 4b^2 \sin(2\theta) \cos(2\theta)]}{[\cos(\theta) + b^2 \cos^3(\theta)]^4} \quad (96)$$

$$- \frac{\{2 [1 + b^2 \cos^2(\theta)] + b^2 \sin^2(2\theta)\} 2 [\cos(\theta) + b^2 \cos^3(\theta)] [-\sin(\theta) - 3b^2 \sin(\theta) \cos^2(\theta)]}{[\cos(\theta) + b^2 \cos^3(\theta)]^4}$$

$$= \frac{2b^2 [-\sin(2\theta) + \sin(4\theta)]}{[\cos(\theta) + b^2 \cos^3(\theta)]^2} + 2 \frac{\{2 [1 + b^2 \cos^2(\theta)] + b^2 \sin^2(2\theta)\} [\sin(\theta) + 3b^2 \sin(\theta) \cos^2(\theta)]}{[\cos(\theta) + b^2 \cos^3(\theta)]^3} \quad (97)$$

$$\frac{d^3 f(0)}{d\theta^3} = 0 \quad (98)$$

$$\frac{d^4 f(0)}{d\theta^4} = 2b^2 \frac{[1 + b^2]^2 [-2 + 4]}{[1 + b^2]^4} + 2 \frac{[1 + b^2]^3 [2 + 2b^2] [1 + 3b^2]}{[1 + b^2]^6} \quad (99)$$

$$= \frac{4b^2}{[1 + b^2]^2} + \frac{4 [1 + 3b^2]}{[1 + b^2]^2} \quad (100)$$

$$= \frac{4 + 16b^2}{[1 + b^2]^2} \quad (101)$$

E Metropolis Monte Carlo code for the thickness optimization

```

import numpy as np
import random
from matplotlib import pyplot as plt
import os
"""
Simulated annealing optimization of the thicknesses of a lens.
"""

def phase(freqs, thickness, deltan):
    """
    Returns the phase shift of a light wave with a certain frequency freq induced by a path through a
    certain thickness
    compared between materials with a difference in refractive index deltan.
    """
    return [thickness * deltan / freq % 1 for freq in freqs]

def get_all_phases(freqs, layers, deltan):
    """
    All possible phases shifts of a light wave with a certain frequency freq induced by a path
    through all possible
    thicknesses that are possible to all possible combinations of the layers
    compared between materials with a difference in refractive index deltan.
    """
    num_layers = max(np.shape(layers))
    thicknesses = np.zeros(2 ** num_layers) # get all possible thicknesses
    for i in range(2 ** num_layers):
        thickness = 0
        for j in range(num_layers):
            if i % (2 ** (num_layers - j)) // 2 ** (num_layers - j - 1) != 0:
                thickness += layers[j]
        thicknesses[i] = thickness

    return [phase(freqs, thickness, deltan) for thickness in thicknesses] # get all possible phase
    shifts

def get_closest_phases(phases, ref_phase):
    """
    Makes sure distance between phases takes into account periodicity
    """
    closest_phases = phases
    for i in range(np.shape(phases)[0]):
        phase = phases[i]
        for freq_nr in range(len(phase)):
            if phase[freq_nr] - ref_phase[freq_nr] > 0.5:
                phase[freq_nr] -= 1
            elif ref_phase[freq_nr] - phase[freq_nr] > 0.5:
                phase[freq_nr] += 1
        closest_phases[i] = phase
    return closest_phases

def objective(freqs, layers, deltan, number_of_tests=3e3):
    """
    Returns the RMS of the distance between a point in the phase space and the closest available
    space.
    Needs to be minimised by the thermal anneal.
    """
    number_of_tests = int(number_of_tests)

```

```

nf = len(freqs) # number of frequencies
phases = get_all_phases(freqs, layers, deltan) # get all available phases

obj = 0 # initialization
for i in range(number_of_tests):
    test_phase = np.array([random.random() for i in range(nf)]) # generate random phase
    closest_phases = get_closest_phases(phases, test_phase) # take into account periodicity

    obj += min([np.linalg.norm(test_phase - phas) for phas in closest_phases])**power # add the
        # smallest distance
return (obj / number_of_tests)**(1/power) # mean of squares of average distances

def get_temperature(i, iterations):
    """
    Temperature in function of the steps.
    temperature decreases exponentially during anneal --> it gets increasingly difficult to increase
        the energy
    of the system
    """
    return 5e-3*np.exp(-4 * i / iterations)

if not os.path.exists("./best_layers"):
    # if the demo_folder directory is not present
    # then create it.
    os.makedirs("./best_layers")

max_thicknesses = [0.3, 0.4, 0.5, 0.6] # maximum thickness of a single layer

for num_layers in range(1, 7):
    for max_thickness in max_thicknesses:
        # num_layers = 4 # number of layers to optimize
        power = 2
        frequencies = [0.47, 0.55, 0.65] # frequencies that you want to optimise independently
        # frequencies = [0.6]

        deltan = 2.7 - 1.45 # difference in refractive index

        step_size = 0.1 # size of perturbation in every step

        seed = 111 # makes sure we can reproduce results --> change to get different results
        np.random.seed(seed)

        # initialize starting layer thicknesses and objective
        layers = np.array([random.randint(0, int(max_thickness*1e3))/1e3 for i in range(num_layers)])

        # layers = np.array([0.5, 0.278, 0.087, 0.42])
        # layers = np.array([0.356, 0.255])
        current_obj = objective(frequencies, layers, deltan)
        best_obj = current_obj
        best_layers = layers
        iterations = int(1e4)
        accuracy = int(2e2)
        plt.figure()
        for i in range(iterations):
            T = get_temperature(i, iterations)
            # change_layer = random.randint(0, num_layers-1)
            # old_thickness = layers[change_layer]

```

```

# layers[change_layer] = random.randint(0, int(max_thickness*1e3)) / 1e3 # change layer
# thickness on nm accuracy

# Perturbation on thicknesses:
difference = [step_size*(1-random.randint(0, int(2*step_size*1e3)) / (1e3*step_size)) for
              i in range(num_layers)]
new_layers = [min(max(layers[i] + difference[i], 0), max_thickness) for i in
              range(num_layers)]

# new objective
new_obj = objective(frequencies, new_layers, deltan, accuracy)

# check if energy decreased OR accept increase with certain probability
if new_obj <= current_obj or np.exp((current_obj - new_obj) / T) > random.random():

    print(current_obj - new_obj)
    # adjust new value
    current_obj = new_obj
    layers = new_layers

    if new_obj < best_obj:
        best_obj = new_obj
        best_layers = new_layers

    # plot
    # if len(frequencies) == 2:
    #     plt.clf()
    #     phases = np.array(get_all_phases(frequencies, layers, deltan))
    #     plt.scatter(phases[:, 0], phases[:, 1])
    #     plt.xlim((0, 1))
    #     plt.ylim((0, 1))
    #     plt.title("Objective = " + str(current_obj))
    #     plt.pause(0.00001)

# print progress
if 10*i % iterations == 0:
    print(str(int(i/iterations*100)) + "%")
if (10*i)//iterations == 9:
    step_size = 0.01

accuracy = ((10*i)//iterations+1) * 200
best_obj = objective(frequencies, new_layers, deltan, accuracy)
if current_obj < best_obj:
    best_obj = current_obj
    best_layers = layers

# print result
print(best_obj)
print(best_layers)
phases = np.array(get_all_phases(frequencies, best_layers, deltan))
print(phases)

# save result
with open("./best_layers/best_results_"+ str(power) + "thorder_freq_" + str(frequencies) +
          "_layers_" + str(num_layers) + ".txt", 'a') as var_file:
    var_file.write("objective \t" + str(best_obj) + "\n")
    var_file.write("best_design \t" + str(best_layers) + "\n")
    var_file.write("phases \t" + str(phases) + "\n")

# plot result

```

```
if len(frequencies) == 2:  
    plt.figure()  
    plt.scatter(phases[:, 0], phases[:, 1])  
    plt.xlim((0, 1))  
    plt.ylim((0, 1))  
    plt.xlabel("Phase shift for blue [/360]")  
    plt.ylabel("Phase shift for red [/360]")  
    plt.savefig("./best_layers/best_results_" + str(power) + "thorder_freq_" + str(frequencies)  
              + "_layers_" + str(num_layers) + "max_t" + str(max_thickness) + ".png")
```
